

**The Einstein-de Haas Effect in Yttrium Iron Garnet at Radio
Frequencies**

by

Michael George Dunsmore

A thesis submitted in partial fulfillment of the requirements for the degree of

Master of Science

Department of Physics
University of Alberta

© Michael George Dunsmore, 2022

Abstract

The Einstein-de Haas (EdH) effect was measured for the first time more than a century ago, and a classical theory of its operational principle existed many years before the first observation of the effect. EdH torques are generated by the time rate of change of angular momentum and represent the close relationship between magnetism and mechanical angular momentum. This work serves to build upon a trend of miniaturizing EdH experiments, thereby increasing the frequency that EdH torques are applied. The pursuit of extending EdH torques to higher frequency outlines a distinct benefit of the EdH effect: the torque scales linearly in magnitude with drive frequency. This linear scaling of EdH torques is in stark contrast with conventionally studied cross-product torques, which scale linearly with applied DC field and are frequency independent. The first measurement of the EdH effect featured torques that were of order one million times smaller than cross-product torques. Enabled by nanofabrication of mechanical torsional resonators, we have brought measurements of the EdH effect to the nanoscale, and subsequently to radio frequencies where EdH and cross-product torques are of similar magnitude.

Single crystal disks of yttrium iron garnet (YIG) with vortex ground states were affixed to the nanofabricated torsional resonators. Owing to the distinct origin of EdH and cross-product torques, we were able to simultaneously measure the torques and observed relative differences in the signal phases as the field was swept. The DC field where EdH and cross-product torque signals intersect allows us to calculate the magnetomechanical ratio g' for YIG: the first measurement of its kind. Our results yield $g' = 1.78 \pm 0.16$. The uniformity of driving fields allows for the extension of EdH

torque measurements beyond the low field and ultimately beyond annihilation of the vortex state. EdH torques in intermediate and high field ranges serve as a sensitive probe of magnetic surface defects. Future directions of this work are presented with an emphasis on testing the limit of the linear increase of EdH torque with frequency. We suggest that a phase-lag with respect to the driving field will emerge for high enough mechanical frequencies that will signal the out-pacing of spin lattice relaxation times.

Preface

The content of Chapter 1 and Chapter 3 are an original work by Michael Dunsmore. No part of these chapters has been previously published.

Figures 2.5, 2.6, 2.7, 2.8, 2.10, 2.11, 2.12, 2.13, 2.14, and 2.15 found in Chapter 2 of this thesis have been published as part of K. Mori, M. G. Dunsmore, J. E. Losby, D. M. Jenson, M. Belov, and M. R. Freeman, “Einstein–de Haas effect at radio frequencies in and near magnetic equilibrium”, *Phys. Rev. B*, vol. 102, p. 054415, 5 2020, doi:10.1103/PhysRevB.102.054415. I was responsible for the design and simulations of the driving coils, COMSOL simulation analysis of resonator degree of torsionality, code for the toy model of coupled translational and torsional mode, thermomechanical calibration, analysis of data, writing and analysis of some mumax3 simulations, as well as figure creation. K. Mori was responsible for the data collection and assistance with driving coil design and creation. J. E. Losby constructed the apparatus, and manufactured the nanomechanical resonators. D. M. Jenson assisted with creation of Figures and mumax3 simulations. M. Belov created the YIG disk via focused ion beam milling and placed it on the resonator. M. R. Freeman was the supervisory author and was involved with concept formation and manuscript composition.

“Wonder. Go on and wonder.”

-William Faulkner, The Sound and the Fury

I dedicate this work to Alethia, Garrett, and Darren.

Acknowledgements

I am extremely grateful for the opportunity I have had to work in the field of spin mechanics. I must first thank my supervisor, Mark Freeman, for his support over the years and for fostering an environment of creativity and academic freedom within our group. Mark has also allowed me to attend many conferences that have greatly diversified my learning experience.

I owe a great debt to those I have worked alongside throughout the years. I thank Kayte Mori for her friendship. Without Kayte's exceptional data collecting, this thesis would not have been possible. I offer my gratitude to Katryna Fast, for her efforts editing this thesis, and for her friendship. John Thibault has been a fantastic person to work alongside, and always inspires me with his expert machining skills and his remarkably curious brain. I am very grateful for the long discussions about quantum mechanics I have had in the hallways with Clinton Potts. Thank you to Vince Sauer, Joe Losby, and Miro Belov, who continue to be exceptional mentors. I also owe thanks to John Davis and Al Meldrum who have sat on my committee.

Thank you to all of my friends and family, who formed a tight support circle for me when I needed encouragement. I am grateful for my hiking partners who have always reminded me how big the world is. I would also like to thank Thomas Pynchon, William Faulkner, Ingmar Bergman, and Stephen Malkmus for stimulating the artistic side of my brain.

Table of Contents

1	Introduction to Magnetism	1
1.1	Background	1
1.1.1	Early History	1
1.1.2	Classical Theory of Magnetism	2
1.1.3	Magnetism at the Beginning of the 20th Century and Beyond	3
1.1.4	Magnetic Ordering	5
1.1.5	Ferrimagnetism and Yttrium Iron Garnet	6
1.2	Manifestations of Magnetic Torque	8
1.2.1	Cross-Product Torque	8
1.2.2	Einstein-de Haas Torque	10
1.3	Torque Magnetometry	13
1.4	Micromagnetism	16
1.4.1	The Landau-Lifshitz-Gilbert Equation	17
1.4.2	Case Studies of Spin Texture: The Vortex and Quasi-uniform State	21
2	The Einstein-de Haas Effect at Radio Frequencies	24
2.1	Miniaturization of Einstein-de Haas experiments	25
2.2	Apparatus	27
2.2.1	Micromachined Mechanical Devices	27
2.2.2	Optical Interferometry	28
2.2.3	Electronics	30

2.2.4	Static and Driving Field Geometry	31
2.2.5	Mechanical resonances of torsional resonators and degree of torsionality (DoT) calculation	35
2.2.6	Toy Model of Coupled Torsional and Translational Modes	37
2.2.7	Thermomechanical Torque Calibration	40
2.3	Experimental Results and Calculation of the Magnetomechanical Ratio g'	43
2.3.1	Characterization of Mesoscopic YIG Disk Active Magnetic Volume	45
2.3.2	Frequency Dependent Measurement of EdH and Cross Product Torques	49
2.3.3	Simultaneous Measurement of Cross-product and EdH Torques	51
2.3.4	Einstein-de Haas Torques at Larger DC Field Magnitudes and Beyond Vortex Annihilation	54
2.3.5	Micromagnetic Simulations of Einstein-de Haas Experiments	59
3	Conclusions & Future Work	62
3.1	Conclusions	62
3.2	Future Work	63
3.2.1	Spin-Lattice Relaxation from the Perspective of the Lattice	63
3.2.2	Time Rate of Change of Angular Momentum in Superconductors	64
3.2.3	Six-‘axis’ AC Torque Magnetometry	65
	Bibliography	66
	Appendix A: Equivalence of Cross Product and Energy Differential Torque	70
	Appendix B: Sample Code for Macrospin Simulation	72
	Appendix C: Sample Code for Toy Model Simulation	75

List of Figures

1.1	Three common examples of magnetic ordering at low temperature. The leftmost panel is a microscopic example of spin ordering in a ferromagnet. The magnitude of the volume average of each spin's magnetic moment gives the saturation magnetization. The centre panel shows antiferromagnetic order. Here the anti-alignment of magnetic moments produces a vanishing volume average magnetization. The right most panel shows ferrimagnetic ordering. A ferrimagnet has nonzero volume average magnetization despite the antiferromagnetic spin order. . . .	5
1.2	Plots for consideration of cubic magnetocrystalline anisotropy of YIG. The above plots were created for $K_{1,c} = -620 \text{ J/m}^3$ and $K_{2,c} = -5 \text{ J/m}^3$. Panel a) and b) show the cubic anisotropy energy density surface. Panel b) in particular shows a cross section of the energy density surface that is plotted against polar angle ϕ in panel c). The first order derivative of the energy density with respect to polar angle is shown in panel d).	6
1.3	A diagram showing the directions that fields should be applied to induce a torque along the y -axis. A DC field is applied to magnetize the cylinder in the positive x direction, an RF driving field is applied along the z axis so the resulting torque is along y	9

1.4	An individual magnetic moment, \vec{m} , with angular momentum \vec{L} , generated by an orbiting electron in the presence of an externally applied field \vec{H}_{ext} . Panel a) shows the field pointing towards the top of the page, the current in the loop is applied in the clockwise direction to create a magnetic moment that also points towards the top of the page. Additionally, the angular momentum generated by the orbital motion is aligned with the magnetic moment. In panel b) the field is reversed, and crucially so is the direction of rotation. Panel c) shows how an EdH torque can be generated in a thin cylindrical ferromagnet.	10
1.5	Two examples of torque magnetometers. Panel a) represents a traditional DC torque magnetometer where the sample is positioned along the torsion arm, and by applying external fields at different angles, the torque is nulled. Panel b) represents the deceptively simple EdH experimental schematic. A ferromagnetic rod is hung from a torsion wire and surrounded by a coil. The application of an alternating field changes the magnetization direction of the rod, thus inducing a rotation. Panel a) is used with permission from Cullity and Graham's text, Introduction to Magnetic Materials [15] and panel b) is used with permission from Magnetism in Condensed Matter by Stephen Blundell [16].	14
1.6	Simulation output from macrospin simulation of an isotropic sphere with a uniaxial anisotropy axis along the x axis.	20

1.7	<p>Results of micromagnetic simulations in the low and high field regime. The colour represents the angle with which the spins are pointing in the plane. A grayscale indicates the direction of spins out of the plane. Panel (a) shows the highly demagnetized vortex state. The core of the vortex is notably white indicating an out-of-plane magnetization. Panel (b) shows a quasi-uniform spin texture where an external field is applied towards the right hand side of the page. Slight changes in colour and spin direction can be seen close to the edges. These regions are known as closure domains.</p>	21
2.1	<p>Fundamental torsion mode simulated with COMSOL Multiphysics software [35]. The asymmetry of the displacement magnitude is indicative of an admixture of torsional and out-of-plane translational eigenmodes. This admixture arises from the proximity of these two deformational modes in frequency and from asymmetries of mass distribution about the torsion axis the sensor. Figure used with permission from [33]. . .</p>	28
2.2	<p>Schematic displaying the optical circuit and principle of how optical interferometry is used to detect small displacements of the resonator paddle. Panel a) displays the path of the laser from the HeNe laser, to the sample chamber. Panel b) shows the beam emerging from the objective lens as it illuminates the paddle. Several rays are drawn showing portion of the beam that is transmitted through, and reflected off the paddle. Panel c) shows the case where the paddle has been displaced by some torque. The transmitted beam has approximately the same path length as in panel b), however the reflected beam travels a significantly shorter distance.</p>	29

2.3 Electrical diagram of apparatus. We take advantage of two channels of a Zurich UHF lock-in amplifier. The two channels are output at frequencies that are detuned from the mechanical resonance frequency by ± 200 Hz. The two outputs are each sent through a Minicircuits LZY-22+ amplifier, and then to their respective coils. The photoreceiver signal is sent to the input of the lock-in amplifier. 31

2.4 Cartoon schematic of the side and top view of the experimental apparatus. The NdFeB magnet is used for high field hysteresis studies of the YIG disk. This magnet was mounted on a digitally controlled linear translation stage. For finer DC field sweeps, we implement hand-wound electromagnetic coils. 32

2.5 Panel a) shows the PEEK assembly on the vacuum stage. Panel b) and c) show sniffer coil orientations for measurement of relative inductive field strengths for y and z respectively. d) and e) show COMSOL simulated field angle deviations from the y and z directions. The white cube at the centre of the field deviation surface plot is roughly representative of the sample size; thus confirming the uniformity of the field over the volume of the sample. Figure used with permission from [33]. 33

2.6 A torsional eigenmode that is rotating about an axis that is not the centre of the paddle can be thought of as an addition of a pure translational displacement, and a purely torsional displacement. 36

2.7 A toy model of coupled resonances is illustrated in panel a) where a torsional spring with spring constant κ is coupled to a linear spring with spring constant k through a third spring with spring constant $K = \epsilon k$. The displacement from equilibrium position is represented by $x_1 \approx R_{\text{eff}}\theta$ and x_2 . Panel b) and c) represent solutions to Equation 2.6 for various driven frequencies. Measurements of displacements represent deflections of each spring due to some stimulus of a driving torque. Figure used with permission from [33]. 38

2.8 A squared fit to the response of an undriven thermomechanical frequency sweep measured with a 46 Hz noise equivalent power bandwidth. The resonant frequency is $f_0 = 2.79092 \pm 0.00007$ MHz, and the mechanical resonance quality factor is $Q = 1300 \pm 300$. Figure used with permission from [33]. 40

2.9 Calibrated fit to a driven cross product torque signal. The resonant frequency is 2.793452 ± 0.000008 MHz, the quality factor, Q , of the resonance is 1930 ± 20 . Just two standard deviations different from the value obtained in the thermomechanically driven signal. 43

2.10 Experimental (panel a) and simulated (panel b) hysteresis loops generated by the cross-product torque from the YIG disk. Two linear fits are applied to the each hysteresis curve: one to the low field vortex regime, the other to the high field quasi-static regime. The intersection of these curves (indicated by the dashed line) is a sensitive probe of magnetic aspect ratio. 46

2.11 Polar plots of frequency sweeps. The frequency here was swept from 2.75 MHz to 2.84 MHz. The mechanical resonance due to a driving cross-product torque is shown in panel a) and the mechanical resonance due to a driving EdH torque in panel b). The two resonances are, when $\omega = \omega_0$, out of phase by 90° with one another. The true torque phase is given by the orange and green rays for cross-product and EdH torques respectively. The width of the rays represents the uncertainty in phase at the resonance maximum. 49

2.12 Simultaneous measurement of cross-product (driven by H_z^{RF}) and EdH (driven by H_y^{RF}) torques over a range of small bias DC field. The solid lines represent data measured while changing the DC field magnitude. The points represent frequency sweep data at discrete DC field strengths. Discrete frequency sweep measurements offer superior phase SNR than the continuously swept DC field measurement, and therefore are exclusively included in panel b). Panel a) features two intersections of the EdH and cross-product signal that are used to calculate the crossover field, $H_x^{\text{Crossover}}$ 52

2.13 Extension of simultaneous (phase-locked) measurement of H_y^{RF} driven EdH and H_z^{RF} driven cross-product torques throughout the field range that encompasses the vortex state. The field is swept low (L) to high (H) and then H to L. Panels a) and b) represent the unmodified 'raw' magnitude and phase respectively. The linear increase in EdH magnitude and decrease in phase are indicative of cross-product admixture. Panels c) and d) represent the EdH signal where the admixture of cross-product torque has been removed. The remaining features indicate that the EdH torque and phase are sensitive probes of magnetic disorder and surface roughness. The low field phase drift that appears in panel d) is indicative of the PLL losing the reference phase as the signal-to-noise ratio of the cross-product torques becomes too large. 55

2.14 High field hysteresis loops extend to field strengths greater than those that permit vortex spin textures. The irreversible vortex annihilation occurs around 18 kA/m. This spin texture change is observed both in the EdH (as spikes in magnitude and phase) and cross-product torque signals (as discontinuous jumps in magnitude). The spikes that are cut off in panels a) and c) extend to 150 μV . Two magnet rotation positions are shown, 0° , and 1° indicating a striking dependence of bias magnetic field angle on EdH torques. 57

2.15 Simulation outputs for a high field hysteresis measurement wherein cross-product torques are shown in panel a) and EdH torque simulation results are shown in panel b). Bias field offsets of 0.1 kA/m in the y direction are also applied to simulate an applied field at an offset angle. As in the experimental case, this offset has little impact on cross-product torques, however panel b) represents some drastic changes in behaviour between the bias field direction, such as, the large peak around 26 kA/m which is not only unique to the $H_y = 0$ kA/m trace, but is not present in the cross-product torque signal. 60

List of Symbols

Constants

μ_0	Vacuum permeability	1.25663706212(19) N/A ²
e	Elementary charge	$1.60217662 \times 10^{-19}$ C
k_b	Boltzmann's constant	$1.38064852 \times 10^{-23}$ J/K
m_e	Electron mass	$9.10938365 \times 10^{-31}$ kg

Latin

\mathcal{C}_{τ_i}	Thermomechanical calibration factor, for our purposes it is most useful to present in units of aNm/mV
\vec{H}_{ext}	Externally applied field in units of A/m
\vec{J}	Total angular momentum in units of J·s
\vec{M}	Magnetization in units of A/m
\vec{m}	Magnetic moment in units of A·m ²
\vec{S}	Spin angular momentum in units of J·s
E	Energy in units of J
E_{total}	Total energy in units of J
f_{mech}	Mechanical resonance frequency of torsional resonator in units of Hz
g	g-factor; dimensionless
g'	Magnetomechanical ratio; dimensionless

H	Hamiltonian in units of J
H_i^{RF}	Externally applied radio frequency field magnitude applied along a direction i in units of A/m
H_i^{RF}	Externally applied static field applied along a direction i in units of A/m
$H_x^{\text{Crossover}}$	Externally applied static field along the x -axis where the ratio of cross-product and EdH torque is order unity in units of A/m
I	Moment of inertia in units of $\text{kg}\cdot\text{m}^2$
I_i^{RF}	Radio frequency current magnitude applied along a direction i in units of A
$J_{i,j}$ or J	Exchange constant in units of $1/(\text{kg}\cdot\text{m}^2)$
K or k	Linear spring constants in units of N/m
$K_{1,c}$	First cubic anisotropy constant in units of J/m^3
$K_{2,c}$	Second cubic anisotropy constant in units of J/m^3
M_S	Saturation magnetization in units of A/m
N_i	Demagnetizing factor for direction i ; dimensionless
Q or Q_i	Resonance quality factor; dimensionless
R_{eff}	The distance from a rotation axis to the detection location on a torsional resonator in units of m
$S_{\tau_i\tau_i}$	Torque spectral density squared in units of $(\text{N}\cdot\text{m})^2/\text{Hz}$
S_{τ_i}	Torque spectral density in units of $\text{N}\cdot\text{m}/\sqrt{\text{Hz}}$
$S_{\theta_i\theta_i}$	Angular spectral density squared for rotation about an axis i in units of rad^2/Hz
S_{θ_i}	Angular spectral density for rotation about an axis i in units of $\text{rad}/\sqrt{\text{Hz}}$
$S_{V_iV_i}$	Voltage spectral density squared in units of $\text{V}/\sqrt{\text{Hz}}$
S_V	Voltage spectral density in units of $\text{V}/\sqrt{\text{Hz}}$

$S_{x_i x_i}$ Displacement spectral density squared in units of m^2/Hz

S_{x_i} Displacement spectral density in units of $\text{m}/\sqrt{\text{Hz}}$

DoT or DoT_i Degree of torsionality for torque along an axis $i = (x, y, z)$; dimensionless

Greek

α Magnetic disk aspect ratio or Gilbert damping parameter; dimensionless

χ Magnetic volume susceptibility; dimensionless

γ Gyromagnetic ratio in units of $\text{Hz}/(\text{A}/\text{m})$

γ_L Linear damping constant in units of $1/\text{m}$

γ_T Torsional damping constant in units of $\text{J}\cdot\text{s}/\text{rad}$

κ or κ_i^{eff} Torsion spring constant in units of $\text{N}\cdot\text{m}$

ω Angular frequency in units of rad/s

Ψ Total wavefunction used to describe the wavefunction of multiple quantum objects. Units are dependent on selection of basis

ψ_a Single particle wavefunction used to describe the wavefunction of a quantum object with index a . Units are dependent on selection of basis

ρ Mass density in units of kg/m^3

τ DC torque about an axis $i = (x, y, z)$ in units of $\text{N}\cdot\text{m}$

τ^{AC} AC torque about an axis $i = (x, y, z)$ in units of $\text{N}\cdot\text{m}$

τ_i^{EdH} Einstein-de Haas torque about an axis $i = (x, y, z)$ in units of $\text{N}\cdot\text{m}$

$\tau_i^{m \times B}$ Cross-product torque about an axis $i = (x, y, z)$ in units of $\text{N}\cdot\text{m}$

ε Total energy density in units of J/m^3

$\varepsilon_{\text{anisotropy}}$ Anisotropy energy density in units of J/m^3

ε_d Demagnetizing energy density in units of J/m^3

$\varepsilon_{\text{Zeeman}}$ Zeeman energy density in units of J/m^3

Abbreviations

AC stands for alternating current.

DC stands for direct current.

DoT stands for degree of torsionality; also serves as a variable.

EdH stands for Einstein-de Haas.

FIB stands for focused ion beam.

GGG stands for gadolinium gallium garnet.

LLG stands for Landau-Lifshitz-Gilbert.

NdFeB stands for neodymium iron boron.

PEEK stands for polyether ether ketone.

PLL stands for phase locked loop.

RF stands for radio frequency.

YIG stands for yttrium iron garnet.

Chapter 1

Introduction to Magnetism

The central theme of this thesis is magnetism, a deep and complicated subject. This introduction serves to acquaint the reader with the broad strokes of magnetic behaviour that I feel will be of utmost importance for following discussions. I will begin with a whirlwind tour of magnetism throughout history with an emphasis on notable examples of magnetometry, and the development of theories of ferro-, ferri-, and antiferromagnetism. Following this brief description of magnetism in history, our discussion will cover two kinds of torque that are especially important in magnetism: the cross-product torque and the Einstein-de Haas torque. I will then provide a description of experimental techniques of torque magnetometry, and finally I will touch on two important results of micromagnetism: the micromagnetic vortex, and the quasi-uniform state.

1.1 Background

1.1.1 Early History

Magnetism and technological advancement are deeply intertwined subjects. Chinese writing that dates back to 4000 B.C. describe magnetite (or lodestone as it has been historically referred to) and use it to create a primitive compass in 3000-2500 BC. As far as we know, this ancient compass was not used for navigational purposes. By 800 BC, Greek philosophers wrote on the subject of magnetism when it was discovered

that deposits of Lodestone found around Macedonia and Magnesia attracted iron. Chikazumi in his book points out that these peculiarly attractive stones. “[magnetite] could be found in the Magnesia district of Macedonia, and the city of Magnesia in Ionia. The word ‘magnetism’ is believed to originate from these names.” [1]. Humans have relied on magnetic behaviour for navigational purposes since the compass was first used for oceanic exploration. The use of the compass for navigation doesn’t only represent the first of many paradigmatic shifts surrounding the use of magnetism; it also serves as an example of a torque magnetometer. A magnetometer is any device that responds uniquely to magnetic fields. In the case of the compass, the shape of the needle promotes magnetization along the length of the needle. An external field applied at some angle with respect to the length of the compass needle (say the Earth’s magnetic field) will exert a torque that rotates the needle towards the applied field. This torque is perpendicular to the plane in which the magnetization, \vec{m} , and external field, \vec{H}_{ext} , are applied. Thus we may represent this ‘compass needle’ torque as a cross-product relation: $\vec{\tau} = \mu_0 \vec{m} \times \vec{H}_{\text{ext}}$. In this case, the magnetometer tells the user what direction the Earth’s magnetic field is pointing.

1.1.2 Classical Theory of Magnetism

The applicability of magnetism allowed for oceanic navigation, however when the compass was invented, the theory of magnetism was not well-understood. It was not until the nineteenth century when the world of physics saw the genesis of electromagnetic theory, which gave way to the classical theory of magnetic fields. One of the major contributors to the theory of fields was Carl Friedrich Gauss who, in 1832, surprisingly played role of experimenter when he used a torque magnetometer to measure the strength of the Earth’s magnetic field (this is not the last time in this thesis that we will encounter a theorist performing experiments). The account of this measurement is nicely detailed by Malin’s 1982 Nature article [2]. In his first experiment, Gauss suspended a bar magnet from a gold fibre and measured the period of the

magnet's oscillation about the normal. A cross product of compass-needle-like origin induced a torque resulting from misalignment of the magnetic field of the Earth and the bar magnet. The torque imposed on the bar magnet rotated the sample about the axis of the gold fibre. Gauss was able to measure the period of oscillation by affixing a mirror to one end of the magnet which, through a telescope pointed at the mirror, he observed on a linear scale affixed a distance from the magnet. He measured the period of oscillation and Gauss' first result was the magnetic moment of the bar multiplied by the Earth's field (mH). Next, Gauss measured the ratio of the magnetic moment to the Earth's field by recording the deflection of a suspended bar magnet when a second, perpendicular, magnet is introduced. By assuming dipolar scaling of attraction strength, Gauss had measured the ratio m/H . By multiplying the result for m/H to his first result both m and H could be calculated. Gauss' result was the first of many subsequent measurements of the Earth's magnetic field, however this experiment bears a striking resemblance to modern magnetic torque magnetometers. Section 1.3 will explore ways that torque magnetometers can be used to tell us about important magnetic phenomenon.

1.1.3 Magnetism at the Beginning of the 20th Century and Beyond

With the culmination of classical electrodynamics being marked by the formulation of Maxwell's equations, theories about the origin of magnetism in materials was still mysterious. Classical magnetostatic theories did a good job explaining how magnets interacted, but did not explain the emergence of magnetic behaviour. Ampère hypothesized that electrons orbiting atoms could act like small loops of current, the volume average of which would generate a net magnetic field. As we will see soon, this theory was the impetus for Einstein and de Haas' 1915 experiment, and the two were quite convinced that their experiment had proven the existence of these molecular current loops [3]. However, open questions of magnetic behaviour remained. In

his 1911 thesis, Niels Bohr showed that thermal averaging of classical spins cannot produce a nonzero magnetization, thereby stating that ferromagnetism should not be possible under theory of classical physics [4]. This fact was brought up once again in 1921 by Hendrika Johanna van Leeuwen [5]. A theorem was formalized based on this anomaly of classical statistical mechanics by Van Vleck and was called the Bohr-van Leeuwen theorem [6]. At the time of the Bohr-van Leeuwen theorem's publication, quantum mechanics was in its infancy, and would thankfully soon serve to demystify qualities of magnetic behaviour that classical physics was not capable of explaining.

The theory of ferromagnetism could uniquely be described by the exchange interaction, introduced by statistics of identical objects in quantum mechanics. Consider the wavefunction of two indistinguishable quantum objects (a and b) that are close to one another, so their wavefunctions overlap. The wavefunction describing this superposition is

$$\Phi = \frac{1}{\sqrt{2}} \left(\phi_a(\vec{r}_1)\phi_b(\vec{r}_2) \pm \phi_b(\vec{r}_1)\phi_a(\vec{r}_2) \right). \quad (1.1)$$

For fermionic particles, the exchange must be antisymmetric (so we use the $-$ of the \pm), and bosons follow symmetric exchange (so the wavefunction is described with the $+$). The exchange interaction forces spins to either align or anti-align depending on the sign of an exchange constant, J . Quantum mechanically, we describe this effect using the Heisenberg Hamiltonian,

$$H = -2 \sum_{i>j} J_{i,j} \vec{S}_i \cdot \vec{S}_j. \quad (1.2)$$

Here the Heisenberg Hamiltonian is generalized for N particles in a solid. It is worth noting that the Heisenberg Hamiltonian does not explain effects that emerge due to spin orbit interactions, so an additional contribution must be included to describe this behaviour. An important property of magnetic systems that is not accounted for by the Heisenberg Hamiltonian is magnetocrystalline anisotropy, which is largely treated phenomenologically within the continuum approximation, though first principle calculations do exist [7].

1.1.4 Magnetic Ordering

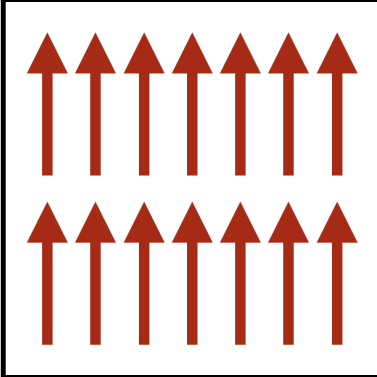
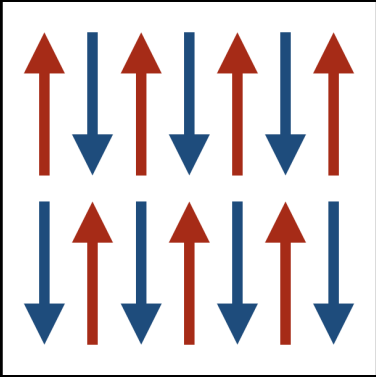
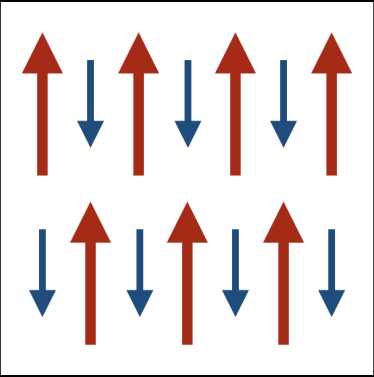
Ferromagnetic ordering	Antiferromagnetic ordering	Ferrimagnetic ordering
		
$ \vec{M} = M_s$	$ \vec{M} = 0$	$ \vec{M} \neq 0$

Figure 1.1: Three common examples of magnetic ordering at low temperature. The leftmost panel is a microscopic example of spin ordering in a ferromagnet. The magnitude of the volume average of each spin’s magnetic moment gives the saturation magnetization. The centre panel shows antiferromagnetic order. Here the anti-alignment of magnetic moments produces a vanishing volume average magnetization. The right most panel shows ferrimagnetic ordering. A ferrimagnet has nonzero volume average magnetization despite the antiferromagnetic spin order.

The exchange constant, J , presented in equation 1.2 plays a significant role in spin ordering, by selecting a particular sign of J we observe dramatic differences in magnetic ordering. We will consider a few examples of J . Let us begin with a positive exchange constant ($J > 0$). We find that each spin is aligned with its neighbours, which we call ferromagnetic ordering (leftmost panel of Figure 1.1). In this case, the net magnetization throughout the volume of the sample is nonzero. A negative exchange constant ($J < 0$) gives rise to anti-aligned neighbouring spins, known as antiferromagnetic ordering (centre panel of Figure 1.1). It is convenient to consider antiferromagnetism as two equal and oppositely oriented ferromagnetically ordered sublattices. An example is given in Figure 1.1 where the sublattices are colour-coded. The magnitude of the volume average of magnetic moment results in a vanishing contribution to the net magnetization.

1.1.5 Ferrimagnetism and Yttrium Iron Garnet

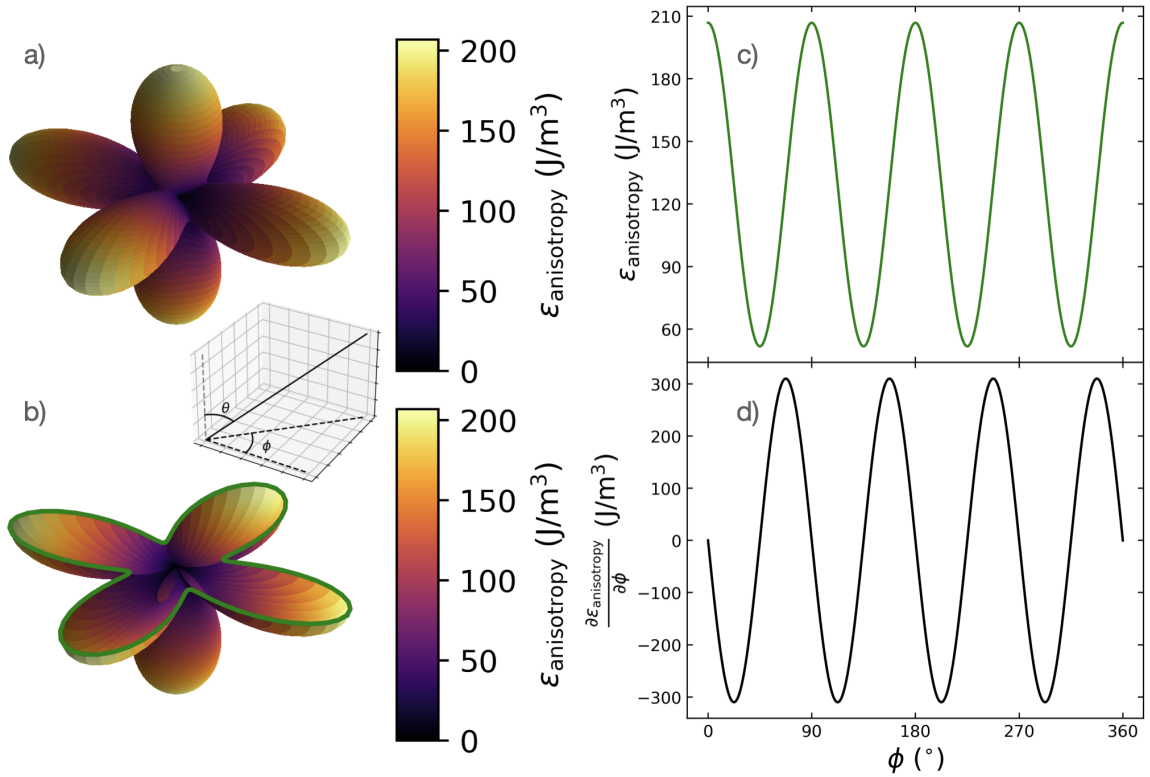


Figure 1.2: Plots for consideration of cubic magnetocrystalline anisotropy of YIG. The above plots were created for $K_{1,c} = -620 \text{ J/m}^3$ and $K_{2,c} = -5 \text{ J/m}^3$. Panel a) and b) show the cubic anisotropy energy density surface. Panel b) in particular shows a cross section of the energy density surface that is plotted against polar angle ϕ in panel c). The first order derivative of the energy density with respect to polar angle is shown in panel d).

Ferromagnetism and antiferromagnetism are not the only kinds of magnetic ordering that are possible. For the purpose of this thesis, we will be especially interested in ferrimagnetic ordering, where two oppositely magnetized sublattices are present (as in an antiferromagnet) however the average magnetization of each sublattice is not equal. Therefore the combination of the two sublattices has a nonzero average magnetization despite antiferromagnetic microscopic ordering. Ferrimagnetic ordering is illustrated in the rightmost panel of Figure 1.1. The nonzero average magnetization could be due to a smaller number of magnetic atoms on one of the two sublattices, or simply the atoms on one lattice could contain a different magnetic moment from

those on its antialigned counterpart. We can treat a ferrimagnet like a ‘soft ferromagnet’; a material or structure that is ferromagnetically soft is similar to a ferromagnet, but has a relatively low anisotropy allowing the material to easily demagnetize. We may compare this to a typical ferromagnet like Neodymium Iron Boron (NdFeB), which is a material frequently used to create exceptionally strong permanent magnet. Permanent magnets harbour large anisotropy and as a result, are very difficult to demagnetize. This is in stark contrast with a soft ferromagnet that demagnetizes easily due to its relatively small anisotropy constants. The magnitude of the anisotropy is given by anisotropy constants K , that have dimension of J/m^3 . A notable example of a ferrimagnet that is often treated as a soft ferromagnet is the ferrite insulator, yttrium iron garnet ($\text{Y}_3\text{Fe}_5\text{O}_{12}$, commonly referred to as YIG). YIG has a weak cubic magnetocrystalline anisotropy that hosts 4 easy axes of magnetization, and 3 hard axes since it has negative anisotropy constants $K_{1,c}$ and $K_{2,c}$. It is useful to consider anisotropies in terms of the anisotropy energy density, $\varepsilon_{\text{anisotropy}}$ expressed as an expansion of magnetization directions in spherical coordinates

$$\begin{aligned} \varepsilon_{\text{anisotropy}} = & K_{1,c}(\sin^4(\theta) \cos^2(\phi) \sin^2(\phi) + \cos^2(\theta) \sin^2(\theta)) \\ & + K_{2,c}(\sin^4(\theta) \cos^2(\theta) \sin^2(\phi) \cos^2(\phi)). \end{aligned} \tag{1.3}$$

We have assumed the usual spherical coordinate convention, so θ and ϕ are the azimuthal and polar angles respectively. The energy density surface show in Figure 1.2 gives us useful insight into the anisotropic behaviour of YIG. Panel a) and b) show the energy density surface. The lobes along the x , y , and z directions correspond to ‘hard’ axes, while surface minima, found along the diagonals, correspond to ‘easy’ axes of magnetization. To magnetize along a hard axis, a large field must be applied since there is a significant anisotropic energy. The easy axis will preferentially be magnetized at lower field strength. A cross section of the surface is shown in panel b) of Figure 1.2, and plotted against polar angle in panel c). We will see in due time that the derivative of the anisotropy energy with angle represents the cross-product torque so the first order derivative of energy with respect to polar angle is presented

in panel d). We see that the torque goes to zero at energy extrema. Naturally, we may consider the use of the torque as a probe of the magnetic energy density.

In addition to its ideal soft-ferromagnetic behaviour, YIG has impressively low damping and, as such, a reasonably high spin resonant quality factor, Q . In 1957, Geller and Gilleo synthesized single-crystal YIG for the first time [8], paving the way for studies on high purity YIG samples. Low damping, coupled with availability of single crystal YIG samples make it an ideal material for studying spin dynamics and magneto-optics.

1.2 Manifestations of Magnetic Torque

For the purposes of this thesis, we should begin with a distinction between two kinds of magnetic torque. The first kind of torque is the earliest observed torque, that is the ‘compass-needle’ or cross product torque. The second kind of torque that we will discuss is the Einstein-de Haas (EdH) torque, which is a direct result of angular momentum conservation within a magnetic system. In the remainder of this section, I will present each torque’s distinct origin, and give a history of notable experimental results.

1.2.1 Cross-Product Torque

Cross product torque arises when the magnetization direction \vec{m} is not along the same direction as a magnetostatic field, \vec{H} . Contributions to \vec{H} may be due to anisotropy, demagnetizing field, and externally applied field. The magnetic torque is written in the recognizable form $\vec{\tau} = \mu_0 V \vec{m} \times \vec{H}$ where μ_0 is the vacuum permeability. Figure 1.3 shows a way in which an AC cross-product torque can be applied along the y -axis of a cylindrical magnet. In this case, we assume that the magnetization of the cylinder is mostly within the plane due to the influence of demagnetizing fields.

The cross-product torque can also be represented as the derivative of the magnetic energy density, ε , with respect to the angular deviation of the magnetic moment, θ

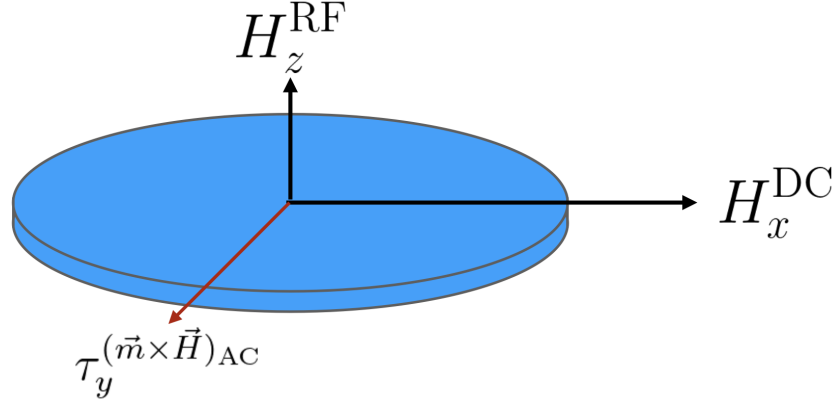


Figure 1.3: A diagram showing the directions that fields should be applied to induce a torque along the y -axis. A DC field is applied to magnetize the cylinder in the positive x direction, an RF driving field is applied along the z axis so the resulting torque is along y .

(for a derivation of this equivalence, see Appendix A). We find

$$\tau = -V \frac{d\varepsilon}{d\theta}, \quad (1.4)$$

where V is the volume of the magnet. Consider the simplest case of a sphere of magnetically-isotropic material, which therefore harbours no contribution to anisotropy. When we apply a magnetic field to the sphere, the energy is given entirely by the Zeeman energy density, ε_Z , which describes the interaction between the magnetization ($\vec{M} = \frac{\vec{m}}{V}$) and a magnetic field \vec{H}

$$\varepsilon_Z = -\mu_0 \vec{M} \cdot \vec{H} \quad (1.5)$$

Since there is no external source of anisotropy, the angle between \vec{m} and \vec{H} is small, therefore in the case where there is no anisotropy, no torque is produced. This places the development of torque entirely upon intrinsic anisotropies, like that of magnetocrystalline nature, or anisotropy introduced by magnetic sample geometry. Since there is no contribution to torque from the Zeeman term, the measurement of cross-product torque is an extremely precise way to understand a material's magnetic anisotropy. Of particular importance for this thesis, is the AC torque which is given

by the second order differential with respect to angle θ

$$\tau^{\text{AC}} = -V \frac{d^2 \varepsilon}{d\theta^2} \frac{d\phi}{dH} |\vec{H}^{\text{AC}}| \quad (1.6)$$

where ϕ is the angle created between the DC field, \vec{H}^{DC} , and the modulated, AC field (I will occasionally refer to this as the dither field), \vec{H}^{AC} , combined with the DC field $\vec{H}^{\text{AC}} + \vec{H}^{\text{DC}}$. Using the usual cross product relationship we find $\sin(\phi) = \frac{|(\vec{H}^{\text{AC}} + \vec{H}^{\text{DC}}) \times \vec{H}^{\text{DC}}|}{|\vec{H}^{\text{AC}} + \vec{H}^{\text{DC}}| |\vec{H}^{\text{DC}}|}$. For a sufficiently small AC field compared to the DC field, we may use the small angle approximation $\sin(\phi) \sim \phi$. Once again, figure 1.3 shows how this kind of torque can be generated along the y -axis since the driving field draws the magnetization out of the plane of the cylinder. The large curvature of the energy density surface due to the demagnetizing energy term results in a cross-product torque.

1.2.2 Einstein-de Haas Torque

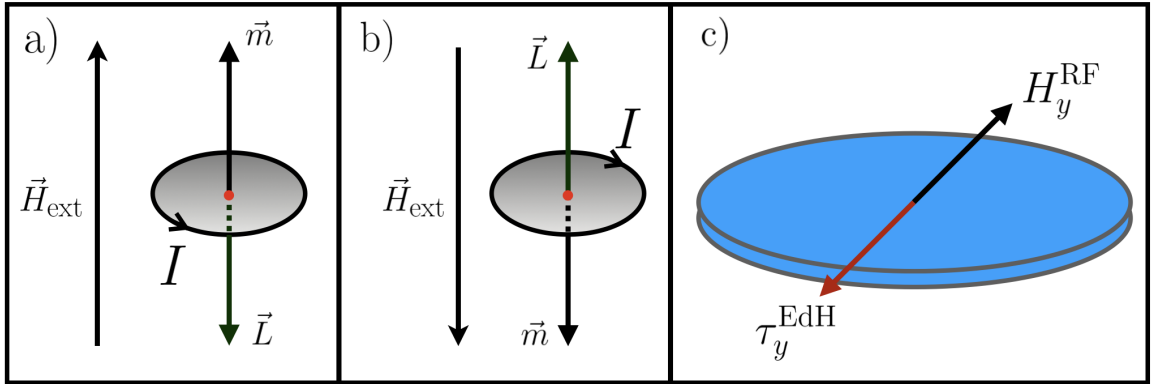


Figure 1.4: An individual magnetic moment, \vec{m} , with angular momentum \vec{L} , generated by an orbiting electron in the presence of an externally applied field \vec{H}_{ext} . Panel a) shows the field pointing towards the top of the page, the current in the loop is applied in the clockwise direction to create a magnetic moment that also points towards the top of the page. Additionally, the angular momentum generated by the orbital motion is aligned with the magnetic moment. In panel b) the field is reversed, and crucially so is the direction of rotation. Panel c) shows how an EdH torque can be generated in a thin cylindrical ferromagnet.

The second kind of magnetic torque we will discuss is the Einstein-de Haas (EdH) torque. Consider, as we did in Section 1.1, Ampère's idea of a molecular current loop.

In this case, the orbiting electron can be thought of as a current of a single elementary charge which generates a magnetic moment. We can obtain the relationship between the magnetic moment, \vec{m} , and angular momentum \vec{L} simply in this toy model. For an orbital radius a , the current is given by that of a current loop $I = \frac{e|\vec{v}|}{2\pi a}$. Since the effective dipole moment is $\vec{m} = \frac{I\vec{A}}{c}$, where \vec{A} is the vector area bounded by the electron's orbit and $\vec{L} = ma(-\hat{I} \times \hat{r})$ for a current and radial unit vectors, \hat{I} and \hat{r} ,

$$\vec{m} = \frac{I\pi a^2}{c}(\hat{I} \times \hat{r}) = \frac{-e}{2mc}\vec{L}. \quad (1.7)$$

Therefore, the magnetic moment is along the same axis as \vec{L} and the two quantities are related through fundamental constants of the electron. If a field is applied to the current loop, the magnetic moment will align with the field, by subsequently reversing the field direction, the moment and angular momentum will follow. The aforementioned process is illustrated in Figure 1.4. The crucial information in this case is the direction of the magnetic moment in the presence of an external magnetic field. For a moment pointing towards the top of the page, an electron must orbit CW, if we then change the field direction, the electron must orbit CCW to create a magnetic moment pointing towards the bottom of the page. Quantum mechanics tells us that the effect of magnetic moment is twofold in an electron-nucleus system: there is the orbital angular momentum, and the electron has its own magnetic moment that is generated by its intrinsic spin angular momentum. Both orbital angular momentum (\vec{L}), and electronic angular momentum (\vec{S}) will contribute to the total angular momentum ($\vec{J} = \vec{L} + \vec{S}$) expended in the process of switching the direction of the applied field. If we now consider the macroscopic example of a ferromagnetic cylinder, which has many magnetic moments that contribute to its total magnetization. Consider the application of a field along the long axis of the cylinder, we can imagine the magnetic dipole moments aligning with the field. If then, the field direction is reversed, the moments will rotate with the field, the spins now take on a different angular momentum value, and by conservation of angular momentum, will contribute angular momentum

to the ferromagnet. Conservation of angular momentum necessarily rotates the magnetic sample to account for this change in field direction. We thus relate the resulting torque about an axis i , τ_i^{EdH} , to the angular momentum J_i by observing the time rate of change of the angular momentum

$$\tau_i^{\text{EdH}} = -\frac{dJ_i}{dt}. \quad (1.8)$$

This effect of rotation was predicted by O.W. Richardson in 1908 [9], however the namesake of the effect is attributed to the first two physicists to successfully observe the effect experimentally: Albert Einstein and Wander Johannes de Haas [3]. A primary goal of EdH experiments is to measure the magnetomechanical ratio g' , which gives the ratio of magnetic moment to angular momentum. Early EdH measurements yielded a notable disagreement in the calculated value of g' . At the time of the first EdH experiment, it was not known that the electron had its own intrinsic spin angular momentum that contributed to the total angular momentum in Equation 1.8. A fascinating historical account of EdH experiments is given in chapter 2 of Peter Galison's book 'How Experiments End' [10]. Experimental consensus was eventually reached sometime in the mid twentieth century owing to experiments by Sucksmith, Barnett, and Scott [11–13], and theoretical investigations disentangling the gyromagnetic ratio, g , from the magnetomechanical factor, g' , by Charles Kittel [14]. In his paper, Kittel expresses

$$g' = \frac{2m_e}{e} \frac{\Delta m}{\Delta J} = \frac{2m_e}{e} \frac{\Delta m_{\text{orbital}} + \Delta m_{\text{spin}}}{\Delta L + \Delta S}. \quad (1.9)$$

This definition of g' is compared to the g-factor, g , which does not depend on spin orbit angular momentum

$$g = \frac{2m_e}{e} \frac{\Delta m_{\text{orbital}} + \Delta m_{\text{spin}}}{\Delta S}. \quad (1.10)$$

This indicates that the magnetomechanical ratio, g' , is smaller than the g-factor, g , since the total angular momentum adds to the denominator of g' . Experimental results have historically shown $g' < g$ [13, 14].

To this day, Einstein-de Haas experiments are an important way to understand consequences of angular momentum conservation in magnetic systems. The mechanism by which angular momentum is transferred from electrons to the lattice is still not a well-understood process and EdH experiments present a natural way to study angular momentum transfer. New avenues of experimental methods such as cavity opto-mechanics, nanofabrication techniques, and the broad availability of RF instrumentation all serve as a host of new tools that are extremely useful for exploring the EdH effect, as we will see in subsequent chapters.

A trend in modern EdH experiments is the miniaturization of torque magnetometers. This miniaturization does two things. First, smaller mechanical structures have higher frequency resonant modes, therefore torques must be applied at higher frequencies. As we can tell from equation 1.8, if we sinusoidally vary the direction of magnetic moments, the torque should exhibit a linear scaling of magnitude with frequency. Second, miniaturization brings the magnetic samples into the regime of micromagnetics (to be discussed further in Section 1.4).

1.3 Torque Magnetometry

We have so far encountered one example of torque magnetometry in Section 1.1: the compass. To reiterate, magnetometers are devices that measure one or more components of a magnetic field or a magnetic moment. The response of a torque magnetometer to a magnetic field, is a mechanical torque. In Section 1.2 we identified that torque magnetometry is an extremely useful tool for understanding magnetic anisotropies, and can be used to study angular momentum conservation in magnetic systems. Early examples of magnetic torque magnetometers were primarily DC magnetometers. A wealth of examples of early torque magnetometers, discussed in Williams' review of torque magnetometer applications [17], were used for measurement of anisotropy energies. This sentiment harkens back to Figure 1.2, wherein the cross-product torque (produced by the angle variation with anisotropy energy density) could give essential

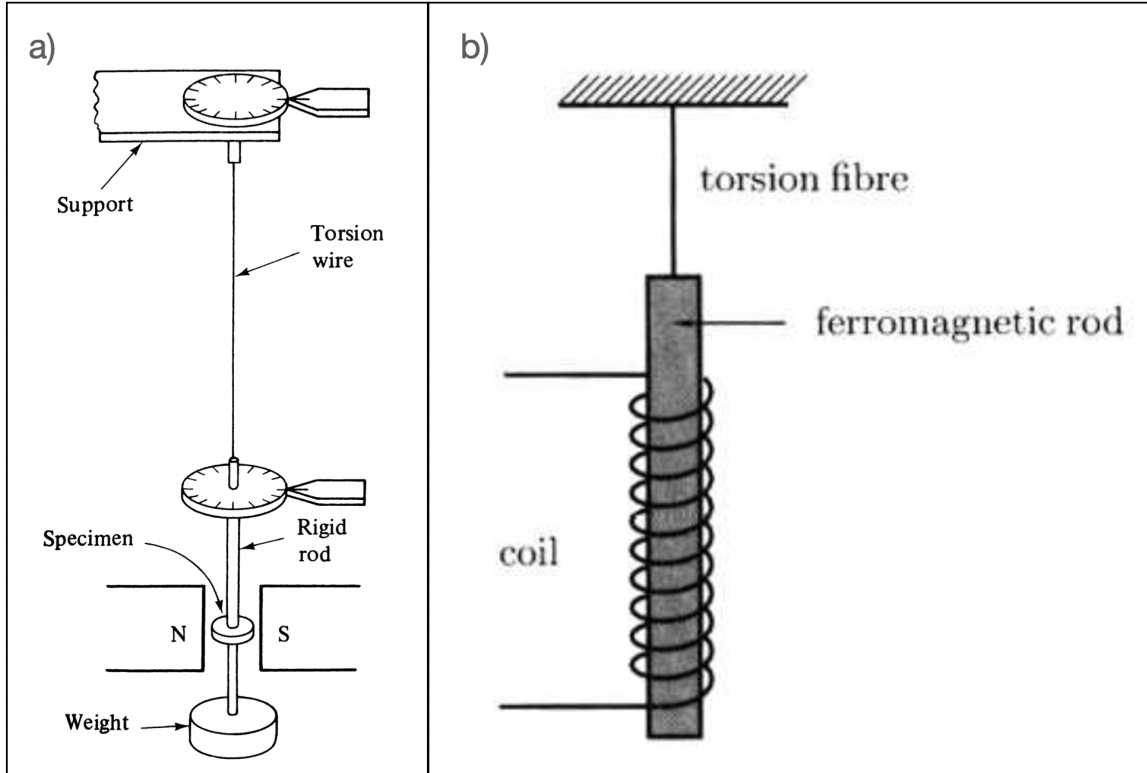


Figure 1.5: Two examples of torque magnetometers. Panel a) represents a traditional DC torque magnetometer where the sample is positioned along the torsion arm, and by applying external fields at different angles, the torque is nulled. Panel b) represents the deceptively simple EdH experimental schematic. A ferromagnetic rod is hung from a torsion wire and surrounded by a coil. The application of an alternating field changes the magnetization direction of the rod, thus inducing a rotation. Panel a) is used with permission from Cullity and Graham's text, *Introduction to Magnetic Materials* [15] and panel b) is used with permission from *Magnetism in Condensed Matter* by Stephen Blundell [16].

information about the location of hard or easy axes of magnetization. Measurements of DC torque on magnetic samples were much more accurate than measurements of magnetization, and it was adopted by the field quickly. An example of the DC torque magnetometer is shown in panel a) of Figure 1.5. Typical operation of a DC torque magnetometer consisted of applying a field which rotated the sample, then applying an opposing mechanical torque to null the effect of the magnetic torque.

Einstein and de Haas, in their 1915 investigation of rotation by magnetization, created an AC torque magnetometer since EdH torques are an exclusively time-varying

effect. A simplified example of an EdH apparatus is shown in panel b) of Figure 1.5. A ferromagnetic rod is suspended from a torsion fibre, and a coil is wrapped around. By running an alternating current through the coil, the magnetization of the rod is modulated, as seen in Section 1.2.2, this induces a mechanical rotation of the ferromagnet. The magnetometer used by Einstein and de-Haas operated at low frequency (49 Hz), partly due to the size of the sample of iron they were studying. This, as alluded to in subsection 1.2.2, means the EdH torque would be extremely small compared to cross-product torques. Subsequent measurements of the EdH effect in the first half of the 20th century were also performed at low frequency

Early EdH experiments were notoriously difficult to perform since there were a host of disturbing factors that interfered with experimental results. Most notably was the measurement of g' . During the first half of the twentieth century, there was considerable debate as to whether g' should be close to 2, or close to unity. One of the reasons there is such a spread in experimental results could be described by the admixture of cross-product and EdH torques. As we will see, phase sensitive measurements of these torques are a smoking gun owing to the 90° phase shift introduced by equation 1.8. In order to disentangle these effects, later experiments went through great effort to eliminate sources of uncertainty [13] and g' was found to be close to 2 for most materials. A 1949 paper written by Charles Kittel [14] gives the relationship between the magnetomechanical ratio, and the spectroscopic splitting factor, g , $2 - g' \approx g - 2$. This is a useful relation since we can predict g' for a material if we know g , which in general is more widely studied.

Silicon micromachining has paved the way forward for development of torque sensors that enable study for a broad host of applications [18]. Quite naturally, microscopic torsional resonators fit into studies of magnetism since the spin angular momentum is intimately related to magnetic materials. Adoption of micromachined torsional resonators for magnetometry grew as availability to microfabrication facilities improved [19–22]. The first micromechanical EdH experiment was performed by

T.M. Wallis, J.M. Moreland, and P. Kabos at NIST [23]. The resonator frequency was 13 kHz, several orders of magnitude larger than foundational EdH experiments, and report a magnetomechanical ratio $g' = 1.83 \pm 0.10$ for permalloy ($\text{Ni}_{80}\text{Fe}_{20}$). Chapter 2 will describe our efforts to further miniaturize the EdH experiment.

1.4 Micromagnetism

The atomistic model of magnetism, while explaining quantum mechanics' role in magnetism, is unable to explain a swath of magnetic behaviour since the Heisenberg Hamiltonian does not account for spin-orbital effects, like spin-phonon interactions, that otherwise could give rise to magnetocrystalline anisotropy and spin-lattice relaxation. William Fuller Brown, Jr. published the theory of micromagnetics in his 1963 book [24], which introduced a phenomenological method for studying magnetic materials. Brown Jr.'s assumption was, for a magnetic specimen that is large enough, the continuum approximation can be introduced, thus neglecting underlying atomic structure and treating interactions classically. In this classical framework, the magnetostatic effects of the magnet can be considered as energy density contributions to the total energy density of the system. Generally speaking, micromagnetism deals with the specific range of magnetic geometries wherein unpredictable domain structure does not form. For the purposes of our discussion, complicated domain structure does not form since our magnetic samples are sufficiently spatially confined. Even though the domain structure is less elaborate than what is found in larger magnetic samples, micromagnetic analysis is nevertheless complicated, with early micromagnetic theory relying on generalizations and simplified modelling. Today, micromagnetism can be studied in the lab thanks to nanofabrication, and thin film deposition; with comparison to experiment made via computational techniques of energy density minimization.

1.4.1 The Landau-Lifshitz-Gilbert Equation

The success of micromagnetism can be expanded on further by introducing dynamical properties of ferromagnets. Dynamics in magnets, commonly known as spin dynamics, is an extremely important subject since widely studied magnetic behaviour, such as spin resonance, cannot be captured without an equation that governs time dependent evolution of magnetic dipoles within a magnetic system. To study dynamics of magnetization, we introduce the magnetization equation of motion: the Landau-Lifshitz-Gilbert (LLG) equation. The LLG equation has a form similar to that of a damped oscillator, the time rate of change of magnetization is equal to two terms, a precession term and a damping term. The equation is as follows

$$\frac{d\vec{M}}{dt} = -\gamma\vec{M} \times \vec{H}_{\text{eff}} + \frac{\alpha}{M_s}\vec{M} \times \frac{d\vec{M}}{dt}, \quad (1.11)$$

where the first term on the right hand side of the equation is the precession term and the second is the damping term; γ is the gyromagnetic ratio, \vec{H}_{eff} is the effective field, α is the Gilbert damping parameter (introduced in 1954, with an addendum published in 2004 [25, 26]), and M_s is the saturation magnetization. An intuitively useful way to present the above equation is by taking a cross product of \vec{M} on both sides to find

$$\vec{M} \times \frac{d\vec{M}}{dt} = -\gamma\vec{M} \times (\vec{M} \times \vec{H}) + \alpha M_s \frac{d\vec{M}}{dt}. \quad (1.12)$$

We may rearrange Equation 1.11 and substitute Equation 1.12 to the damping term such that we may equivalently write

$$\frac{d\vec{M}}{dt} = \frac{-\gamma}{1 + \alpha^2}\vec{M} \times \vec{H}_{\text{eff}} - \frac{\alpha\gamma}{M_s(1 + \alpha^2)}\vec{M} \times (\vec{M} \times \vec{H}_{\text{eff}}). \quad (1.13)$$

Equation 1.13 suggests that the precession term is perpendicular to the magnetic moment, and the damping term is perpendicular to both the moment and precession term. For a three dimensional magnet, the LLG equation is a system of three coupled differential equations in Cartesian coordinates. If we convert the LLG equation to spherical coordinates and assume that the magnitude of magnetization is unchanging

for all times ($M_s = \sqrt{M_x^2 + M_y^2 + M_z^2}$) we may write the LLG equation as two coupled differential equations. We utilize the common substitution of the effective field for the functional derivative of the energy density with respect to the magnetization, $\vec{H}_{\text{eff}} = \frac{\delta E}{\delta \vec{M}}$. These substitutions lead us to the following two coupled partial differential equations

$$\begin{aligned}\frac{dM_\theta}{dt} &= -\gamma M_s \frac{\delta \varepsilon}{\delta M_\phi} - \alpha \frac{dM_\phi}{dt} \\ \frac{dM_\phi}{dt} &= -\gamma M_s \frac{\delta \varepsilon}{\delta M_\theta} + \alpha \frac{dM_\theta}{dt}\end{aligned}\tag{1.14}$$

Where θ and ϕ are the azimuthal and polar angles respectively. The above system of equations can be further simplified by using the Jacobian to exchange the magnetization differentials with angular differentials. We are thus left with the coupled differential equations

$$\begin{aligned}\frac{d\theta}{dt} \sin(\theta) &= -\frac{\gamma}{M_s} \frac{\partial \varepsilon}{\partial \phi} - \alpha \frac{d\phi}{dt} \sin^2(\theta) \\ \frac{d\phi}{dt} \sin(\theta) &= \frac{\gamma}{M_s} \frac{\partial \varepsilon}{\partial \theta} + \alpha \frac{d\theta}{dt}\end{aligned}\tag{1.15}$$

Further simplifying, by inverting the matrix equation, we arrive at a form of differential equation wherein only one derivative of θ or ϕ is included

$$\begin{aligned}\frac{d\theta}{dt} &= \frac{-\gamma}{M_s(1+\alpha^2)} \left(\frac{1}{\sin(\theta)} \frac{\partial \varepsilon}{\partial \phi} + \alpha \frac{\partial \varepsilon}{\partial \theta} \right) \\ \frac{d\phi}{dt} &= \frac{\gamma}{M_s(1+\alpha^2)} \left(\frac{\alpha}{\sin^2(\theta)} \frac{\partial \varepsilon}{\partial \phi} - \frac{1}{\sin(\theta)} \frac{\partial \varepsilon}{\partial \theta} \right)\end{aligned}\tag{1.16}$$

By solving the above equation, we can obtain the behaviour of the magnetization over time.

A key feature of micromagnetism is the ability to predict the influence of various energy contributions on measurements of ferromagnets. Equation 1.16 explicitly depends on the energy density, which can be broken down into several energy contributions. For the purpose of our discussion, we introduce the following energy density terms: the anisotropy energy density ε_a , the demagnetizing energy density, ε_d , classical exchange energy density ε_e and the Zeeman energy density, ε_z . The anisotropy energy density can be dictated by magnetocrystalline anisotropy energy density (an

example of cubic anisotropy was described in Section 1.1.5), or induced anisotropy due to effects such as exchange bias [27]. As was the case for Equation 1.3, the magnetocrystalline anisotropy energy density is typically written in the form of trigonometric terms. The demagnetizing energy density is also sometimes known as the shape anisotropy, or, the contribution to the total energy density of interacting magnetic dipoles. This term plays a significant role in formation of magnetic spin textures which we will describe in Section 1.4.2, and is generally the most computationally expensive task that must be undertaken when solving problems in micromagnetism. The demagnetizing energy density is defined by the equation

$$\varepsilon_d = -\frac{1}{2}\mu_0\vec{H}_d \cdot \vec{M} \quad (1.17)$$

where \vec{H}_d is the demagnetizing field. The demagnetizing energy density depends uniquely on the magnetic sample geometry. Often times magnetic demagnetizing factors, N , are calculated and can be included as a contribution to an effective field given by the relation

$$\vec{H} = \vec{H}_{\text{ext}} - \vec{H}_d = \vec{H}_{\text{ext}} - N\vec{M}. \quad (1.18)$$

The demagnetizing factor can be calculated by solving the differential equation $\vec{H} = -\nabla U$ where U is the magnetostatic potential. Several examples exist for analytic solutions to this equation for the especially relevant case of a cylinder and ellipsoid [28, 29]. We can also study the classical exchange energy density, which is given by

$$\varepsilon_e = A \left(\nabla \frac{\vec{M}(\vec{r})}{M_S} \right)^2, \quad (1.19)$$

where A is the material dependent exchange stiffness. A crucial quality of the exchange energy density, is that it becomes large in regions where the gradient of \vec{M} is large. Finally, the Zeeman energy is the energy of interaction between magnetization and externally applied field as shown in Equation 1.5.

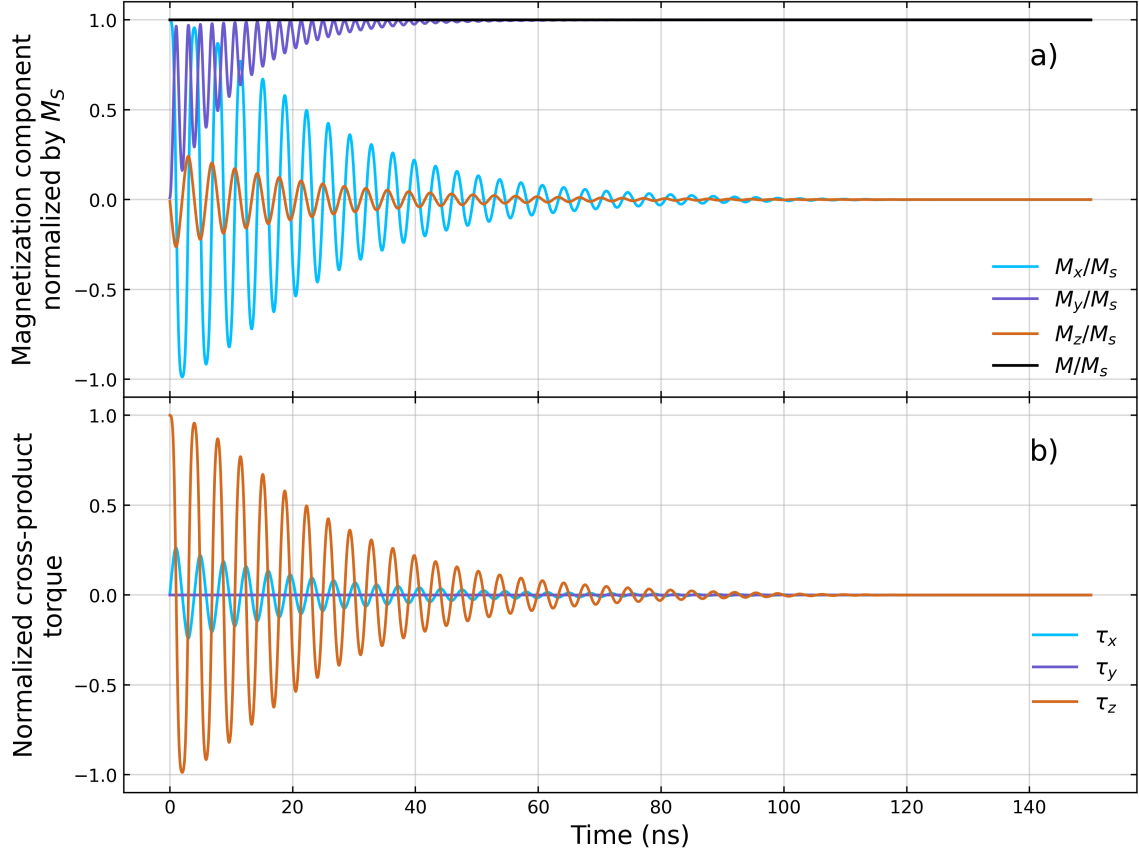


Figure 1.6: Simulation output from macrospin simulation of an isotropic sphere with a uniaxial anisotropy axis along the x axis.

The Macrospin Model

Our mathematical rearrangement of the LLG equation permits integration of the system of coupled differential equations 1.16 using python. The solution to this equation gives the magnetization dynamics and magnetic torque as they evolve in time. In the simple case where we introduce a priori calculated demagnetizing factors to assume shape anisotropy. The solution to this equation thus excludes direct calculation of dipolar influences on neighboring spins, we call this model a ‘macrospin’ model, since we are treating the bulk system as a classical, macroscopic, spin.

From the solutions to equation 1.16 we can represent the magnetization components by using the spherical representation of the Cartesian coordinates. This allows for the simple calculation of the cross-product torque. Figure 1.6 shows the solution to

the macrospin model for an isotropic sphere with no intrinsic anisotropy. Initially, the magnetization is along the x direction, and a static magnetic field is applied along y . The magnetization direction rotates, all the while precessing (indicated by oscillatory behaviour), and eventually comes to rest along the field direction after about 110 ns. In panel b), the cross-product torque is shown. During the precession, the cross product torque about the x and z directions is nonzero. Once the effects of precession have been damped, there is zero torque along all axes, as we predicted in Section 1.2. Solving the LLG equation to the time where the effects of precession are no longer contributing to torques signifies the equilibrium state of the magnet.

1.4.2 Case Studies of Spin Texture: The Vortex and Quasi-uniform State

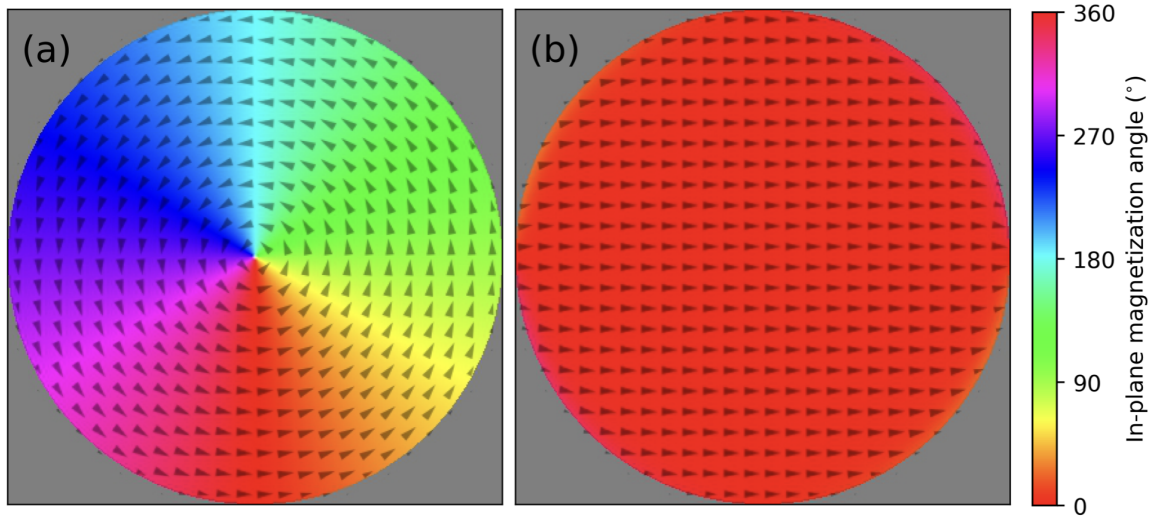


Figure 1.7: Results of micromagnetic simulations in the low and high field regime. The colour represents the angle with which the spins are pointing in the plane. A grayscale indicates the direction of spins out of the plane. Panel (a) shows the highly demagnetized vortex state. The core of the vortex is notably white indicating an out-of-plane magnetization. Panel (b) shows a quasi-uniform spin texture where an external field is applied towards the right hand side of the page. Slight changes in colour and spin direction can be seen close to the edges. These regions are known as closure domains.

Progress in micromagnetism has been greatly accelerated by powerful computa-

tional devices allowing for rapid calculation of systems with ever growing complexity. Calculating the demagnetizing energy, for example, is a particularly computationally expensive task, however one of the beautiful aspects of micromagnetic simulation software is that demagnetizing terms do not need to be known a priori. It is convenient to use geometry provided by electron micrograph, or deposition data, rather than make an analytical calculation for the demagnetizing factors. Today, micromagnetics is commonly performed using finite element model generalizations of the macrospin model. Some examples of notable simulation packages is the CPU-run simulation software, OOMMF [30] and the extremely robust, GPU-run software mumax3 [31]. Parallel computing, enabled by graphical processors, vastly accelerates the already complicated calculations made in micromagnetic simulations and can out-pace even the most powerful CPUs currently available. Since OOMMF does not utilize parallel computing, it tends to be slower so the simulations presented within this thesis will be run through mumax3.

Importantly, micromagnetism introduces the concept of spin texture. Two particular micromagnetic phases will be important for our purposes: the vortex, and the quasiuniform spin textures. The vortex spin texture forms in low fields and largely acts as a demagnetized phase of the ferromagnet. A vortex state is shown in panel (a) of figure 1.7. In the absence of large external field, dipolar interactions of magnetic elements will produce a spin texture that minimizes the field that exists outside of the micromagnet. Around the edges of the magnet, in-plane spin direction is favoured due to demagnetizing energy. In the centre of the magnetic disk, a vortex core forms. The core distinctly exhibits out-of-plane magnetization and a large magnetization gradient promotes large exchange energy density in the core region. This large energy density enhances the core's interactions with its surroundings. Interaction of a vortex core with defects is especially noteworthy [32].

In high fields the vortex structure annihilates, giving way to the quasi-uniform spin texture which can be seen in panel (b) of Figure 1.7. The field is applied in the

positive x direction, which in the present case is to the right hand side of the page. The magnetization is saturated ($M_x \sim M_S$), and several small regions form where spins are not aligned with the applied field. These regions are created due to dipolar interactions and are called closure domains.

Micromagnetism is useful for studies of the EdH effect since micromagnetic simulations can be used to verify relatively uncomplicated spin textures. The spin textures that will be of primary importance here are the micromagnetic vortex state, and the quasi-uniform magnetization state. Keeping with historical tradition, we present our own calculation of g' . The calculation of the magnetomechanical ratio hinges on reliability of micromagnetism, simultaneous measurements of EdH and cross-product torques, and the scaling of torque with frequency as we will see in chapter 2. We expect the spin dynamics predicted by the LLG equation, to be much faster than the mechanical dynamics in the experiment described here, so we will numerically solve the LLG equation out to some distant time where all behaviour of precession has been dominated by the damping. In order to simulate an AC magnetic torque along the y axis, we will have one step wherein the DC field applied along the x direction, then several steps where a dither field along the z direction. A linear fit is applied to the dither and the AC torque can be calculated. Additionally, we calculate the EdH torque along y in a similar way by applying a dither field step along the y , and using the slope of the magnetization variation with dither field we find the EdH torque.

We will see in the following chapter that, in EdH experiments, the vortex core and closure domains become extremely sensitive probes of the surface of magnets. This behaviour is mediated by the unique way in which EdH torques are produced.

Chapter 2

The Einstein-de Haas Effect at Radio Frequencies

The Einstein-de Haas (EdH) effect highlights a deep connection between magnetism and angular momentum. Torque generated as a consequence of the EdH effect is a direct result of the time rate of change of angular momentum in a magnetic system, ultimately enabled by contribution from spin and spin-orbit angular momentum [14], as described in section 1.2.2. The purpose behind many EdH experiments has been the calculation of the magnetomechanical ratio, g' , which represents the ratio of magnetic moment to total angular momentum.

In this chapter, I will begin by introducing a trend in EdH experiments; that is the miniaturization of EdH experiments. I will provide motivation for continuing this trend of miniaturization. A discussion of the experimental apparatus will follow: first I describe the micromechanical torsional resonator and a method of thermomechanical calibration for torsional resonators. Next, I present the design of the RF magnetic field coils and subsequent field phase measurements. Finally a description of optical interferometry is presented. In Section 2.3, I present experimental results with observations of simultaneous measurements of cross-product and EdH torques, calculation of g' , extensions of EdH experiments to higher fields, and comparison of experimental results with micromagnetic simulations. The results of the forthcoming discussion have been published recently in Physical Review B [33], including Figures

2.5, 2.6, 2.7, 2.8, 2.10, 2.11, 2.12, 2.13, 2.14, and 2.15. I was responsible for the design and simulations of the driving coils, COMSOL simulation analysis of resonator degree of torsionality (DoT), code for the toy model of coupled translational and torsional mode, thermomechanical calibration, analysis of data, writing and analysis of some mumax3 simulations, as well as figure creation. K. Mori was responsible for the data collection and assistance with driving coil design and creation. J. E. Losby constructed the apparatus, and manufactured the nanomechanical resonators. D. M. Jenson assisted with creation of Figures and mumax3 simulations. M. Belov created the YIG disk via focused ion beam milling and placed it on the resonator. M. R. Freeman was the supervisory author and was involved with concept formation and manuscript composition.

2.1 Miniaturization of Einstein-de Haas experiments

More than a century has passed since the first measurement of the EdH effect [3]. Following this landmark experiment many more measurements of this effect have been performed [13, 23, 34]. In this section I would like to begin by introducing a particularly interesting trend in EdH measurements: the miniaturization of the experiment. As described in Chapter 1 the EdH effect is a consequence of angular momentum conservation in magnets which translates to a directly observable torque. This torque, τ_i^{EdH} , is defined by the time rate of change of angular momentum, J_i , rotating about some axis, i

$$\tau_i^{\text{EdH}} = -\frac{dJ_i}{dt}. \quad (2.1)$$

If the torque is driven by a sinusoidally varying magnetic field to modulate a component of magnetic moment at frequency ω , with amplitude H_i^{AC} , the angular momentum is modulated at the frequency of the varying magnetic field, $J_i \propto H_i^{\text{AC}} \sin(\omega t)$. The proportionality to amplitude of the driving field implies a linear differential sus-

ceptibility. Therefore we obtain the following proportionality

$$\tau_i^{\text{EdH}} \propto -\omega H_i^{\text{AC}} \cos(\omega t). \quad (2.2)$$

This proportionality reveals a linear dependence between the magnitude and frequency of EdH torque. Additionally, it indicates that the EdH torque is out-of-phase with the driving field by 90° . This phase difference is in contrast with cross-product torques, which are in-phase with the driving field. The relationship between torque magnitude and frequency highlights a significant motivation for miniaturizing EdH experiments: higher frequencies produce larger magnitude EdH torques.

The resonator used in the original experiment by Einstein and de Haas was a cylinder of iron hung from a quartz fibre. The 1915 experiment featured a driving field frequency of 49 Hz. The first major step in EdH effect miniaturization was demonstrated in 2006 by Wallis et al. [23] where g' was measured for a permalloy thin film deposited on a microscale cantilever. Wallis' experiment featured a significant increase in frequency compared to Einstein's work by several orders of magnitude from Einstein's 49 Hz measurement to Wallis' measurement at 13 kHz: the high audio frequency range. The present work miniaturized the Einstein-de Haas experiment even further. The nanoscale torsional resonators we developed brought the fundamental torsional eigenfrequency to the radio frequency range at several MHz [33]. The frequency scaling of EdH torques indicates that the original work of Einstein and de Haas feature torque magnitudes that are as much as a million times smaller than those reported for nanoscale objects. Relative to the corresponding cross-product torques, the work by Wallis features EdH torques that are, relatively, a thousand times smaller than those reported in this thesis. The magnitude of EdH torque compared to conventional cross-product torques is of particular importance for this experiment. We know from Chapter 1 that the cross-product torque depends linearly on DC bias field strength and is independent of driving frequency whereas EdH torques are linearly dependent on driving field frequency. This tells us that extension of cross-product

torque measurements to higher frequencies will not enhance these torque magnitudes. A further discussion of why the comparison of these two torques is essential will be presented in Section 2.3.

2.2 Apparatus

The apparatus that is used for simultaneous measurement of cross-product and EdH torques at radio frequencies consists of several components: the nanoscale torsional resonator, the driving field coil geometry, and the optical interferometer that is used to detect subtle changes in displacement of the nanomechanical resonator. Subsequent sections will describe each of these components, and additionally cover topics of thermomechanical calibration, and phase measurement of excitation coils.

2.2.1 Micromachined Mechanical Devices

Silicon micromachining has allowed for the continuation of EdH experiment miniaturization, the present work features a nano-scale torsional resonator with affixed yttrium iron garnet (YIG) disk. The resonator was created by J. E. Losby using nanolithography and was then transferred to a Hitachi NB5000 focused ion/electron beam (FIB) microscope system. Here, the YIG disks were milled by M. Belov from the YIG thin film layer deposited on a gadolinium-gallium-garnet (GGG) substrate. The disks are approximately $2.2 \mu\text{m}$ in diameter and $0.6 \mu\text{m}$ in height. Such small dimensions are well within the size constraints conducive to a micromagnetic vortex ground state as discussed in Section 1.4. The sides of the disk are not perfectly orthogonal to the z axis because of the angle of incidence of the gallium (Ga) ions used for milling of disks. The process of Ga ion bombardment leaves behind Ga implantation and lattice damage to a depth of order 50 nm, which creates a magnetically inactive region about the disk's perimeter [36]. This leads us to an important step in our analysis whereby conventional cross-product torque hysteresis loops can serve as a sensitive indicator of active magnetic volume (see Section 2.3 for a more complete

discussion of this method).

2.2.2 Optical Interferometry

The motion of our micromachined mechanical resonator was detected by a Fabry-Perot interferometer. We chose an interferometer detection method since it is highly sensitive to exceptionally small displacements of the silicon resonator paddle. The mechanical torques that are produced in our RF EdH experiment, while of comparatively large magnitude due to the high frequency of the driving field, nevertheless generate extremely small deviations in position of the resonator paddle.

Figure 2.2 shows the optical block diagram, and a visual guide for how interferometric detection of resonator displacement was detected. In panel a) we can see that

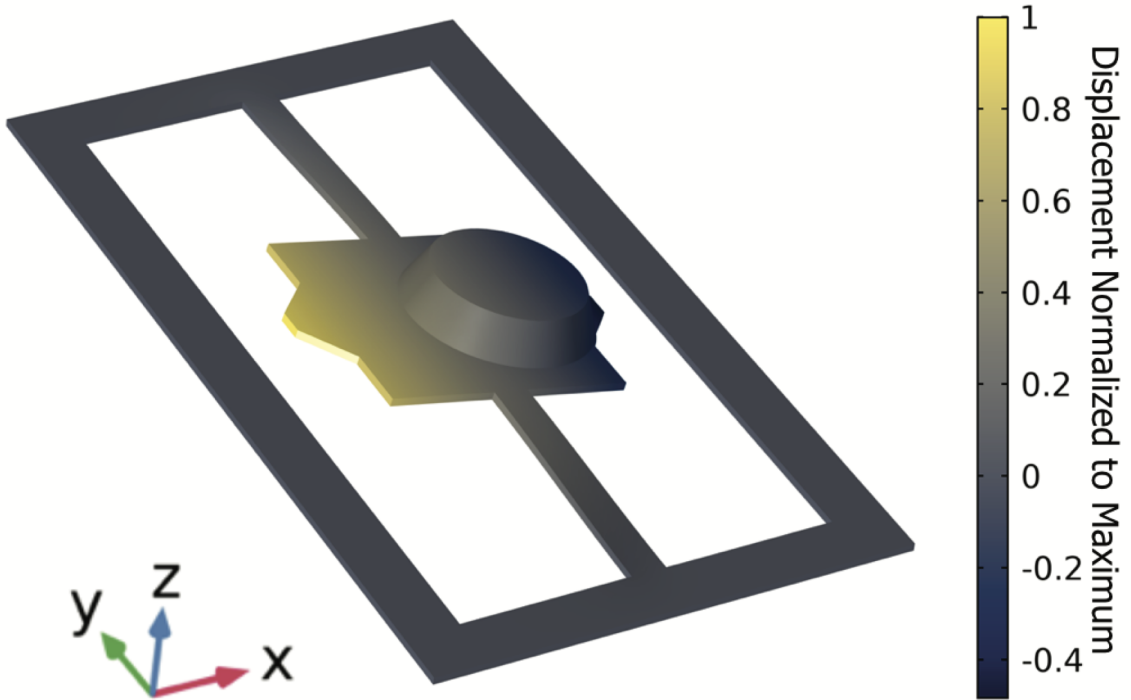


Figure 2.1: Fundamental torsion mode simulated with COMSOL Multiphysics software [35]. The asymmetry of the displacement magnitude is indicative of an admixture of torsional and out-of-plane translational eigenmodes. This admixture arises from the proximity of these two deformational modes in frequency and from asymmetries of mass distribution about the torsion axis the sensor. Figure used with permission from [33].

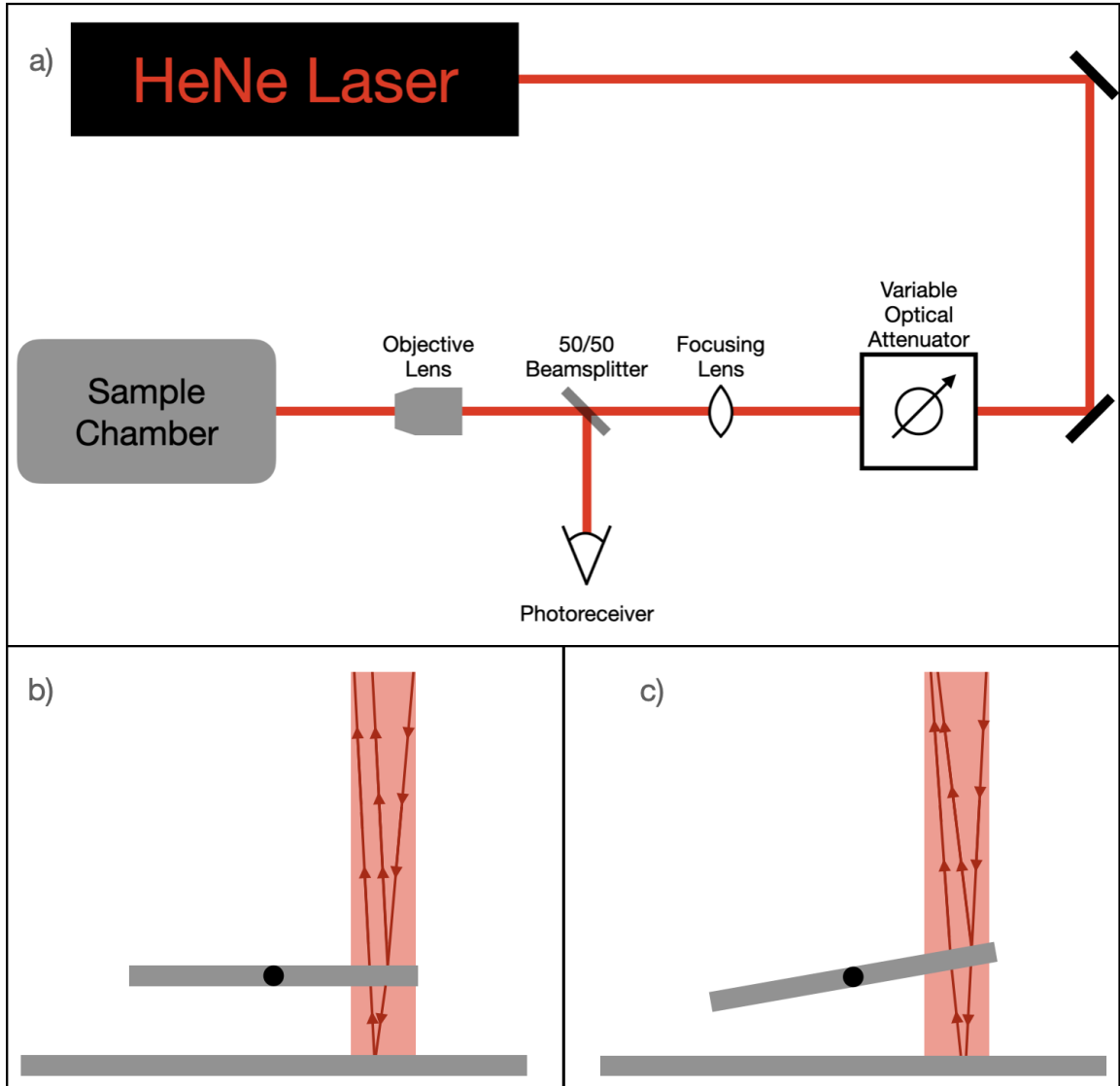


Figure 2.2: Schematic displaying the optical circuit and principle of how optical interferometry is used to detect small displacements of the resonator paddle. Panel a) displays the path of the laser from the HeNe laser, to the sample chamber. Panel b) shows the beam emerging from the objective lens as it illuminates the paddle. Several rays are drawn showing portion of the beam that is transmitted through, and reflected off the paddle. Panel c) shows the case where the paddle has been displaced by some torque. The transmitted beam has approximately the same path length as in panel b), however the reflected beam travels a significantly shorter distance.

A helium-neon (HeNe) laser beam with wavelength 632.8 nm was directed through an optical attenuator. The laser was attenuated before it encountered the device to negate significant effects of laser heating that can affect mechanics and magnetic prop-

erties of the device. A focusing lens is used to overfill the back of the objective lens. The beamsplitter was used to reflect the return beam with signal information into the photoreceiver. The section of the beam pre-interferometer that was reflected off the beamsplitter was terminated in a beam block. The photoreceiver was connected to a Zurich Instruments UHF lock-in amplifier where the signal was demodulated at the drive frequency.

Panel b) and c) serve as visual aids in understanding the principle of interferometry. As shown in panel b) and c), part of the incoming laser beam will be reflected off of the silicon paddle, and part of the beam was transmitted. The reflected part of the beam is similar to the signal arm of a standard interferometer since the position of the reflective surface changes as the magnetic sample imparts a torque on the resonator. The reference arm of this interferometer is the part of the laser beam that was transmitted since the light reflects off of the substrate below, and any motion of the substrate will affect both reference and signal arms equally. The undercut of the resonator was judiciously designed such that its depth was close to an integer number of HeNe laser wavelengths. This means that the space between the resonator paddle and substrate behaves like a low-finesse Fabry-Perot cavity, further enhancing mechanical displacement sensitivity.

2.2.3 Electronics

In order to drive the RF coils, the setup shown in figure 2.3 was used. The multichannel capability of the Zurich amplifier allowed us to maintain a constant separation between the two driving frequencies, detuning them from the mechanical resonance by 200 Hz. The photoreceiver output was plugged into the Zurich amplifier input and the signal containing both the torque signals was demodulated. In measurements of frequency sweeps, like those shown later in figure 2.11, the two frequencies were stepped while maintaining a constant static field and driving field amplitude. To perform hysteresis measurements like those found in section 2.3.3, the frequency

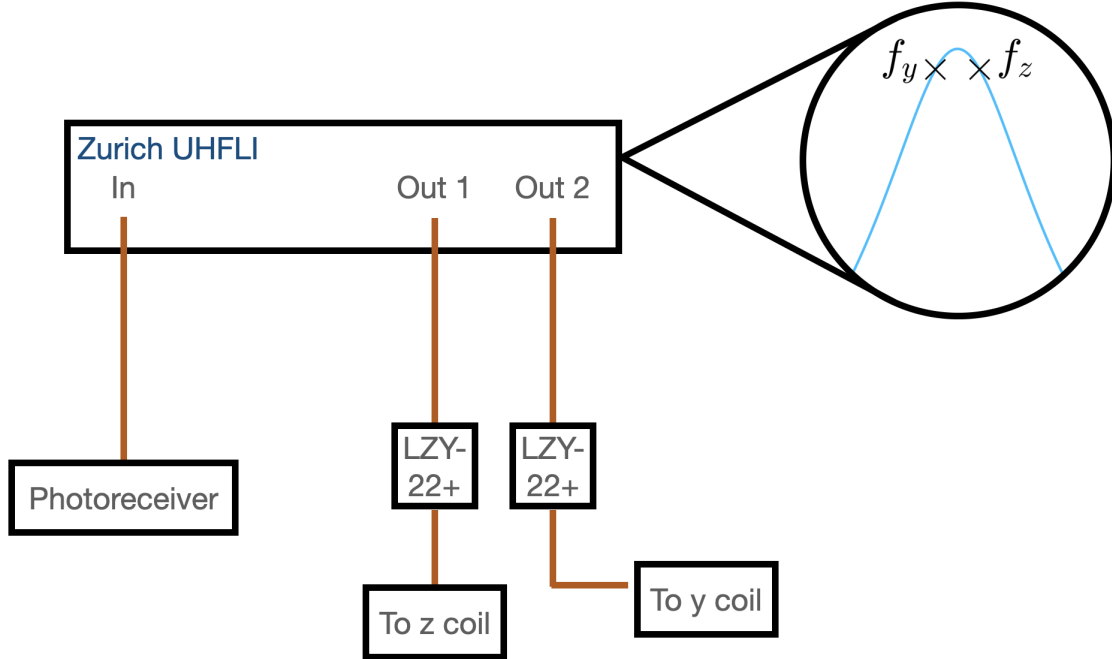


Figure 2.3: Electrical diagram of apparatus. We take advantage of two channels of a Zurich UHF lock-in amplifier. The two channels are output at frequencies that are detuned from the mechanical resonance frequency by ± 200 Hz. The two outputs are each sent through a Minicircuits LZY-22+ amplifier, and then to their respective coils. The photoreceiver signal is sent to the input of the lock-in amplifier.

was held constant while the DC field was changed.

2.2.4 Static and Driving Field Geometry

Static Fields

The application of a static field is essential for generation of cross-product torque as mentioned in Section 1.2. Our apparatus features two ways to apply DC magnetic fields. For high field measurements, a $2'' \times 2'' \times 2''$ neodymium iron boron (NdFeB) permanent magnet is supported on a stepper motor controlled translation stage. Additionally, the NdFeB permanent magnet could be rotated to minimize the influence of stray fields. The permanent magnet was used for high field hysteresis studies of YIG. The low field measurements that will be described in Section 2.3.3 required careful control of DC magnetic field, to achieve this, we implemented two hand-wound

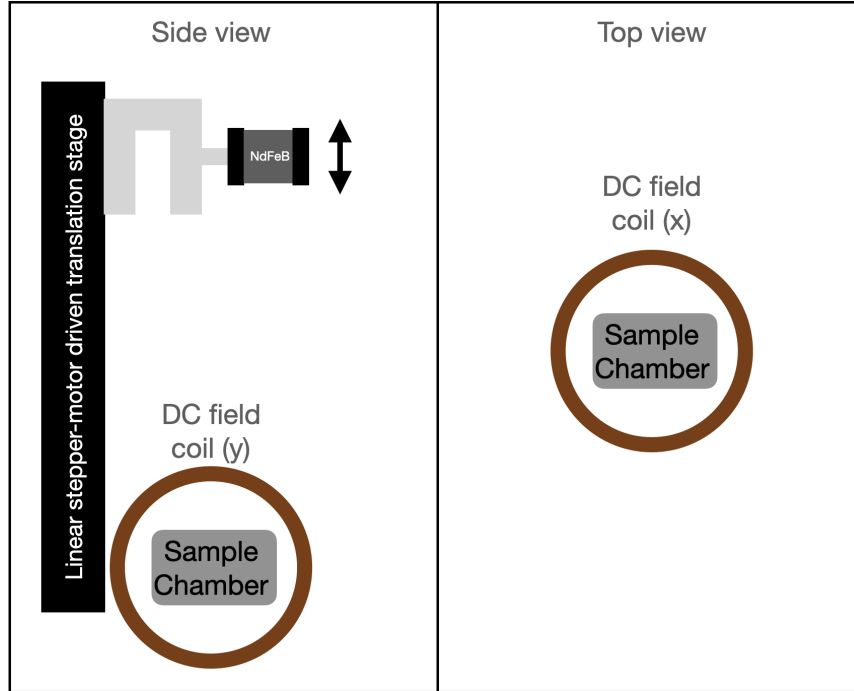


Figure 2.4: Cartoon schematic of the side and top view of the experimental apparatus. The NdFeB magnet is used for high field hysteresis studies of the YIG disk. This magnet was mounted on a digitally controlled linear translation stage. For finer DC field sweeps, we implement hand-wound electromagnetic coils.

air-core electromagnet coils. An Agilent current supply was used to control the current passing through the coils, and a 3-axis Hall probe was used to monitor DC field strengths at a location close to the sample chip.

Driving Fields

Einstein-de Haas and cross-product torques in this experiment were applied along the same axis, but have distinctly different origins. The EdH torque is generated by a field along the torsion axis while cross product torques are generated by a driving field that is out of the plane of the magnetic disk. A significant challenge that we had to overcome was measuring both torques simultaneously. In order to avoid admixture of torsional components, the driving field geometry is of great importance. To drive both torques along the y axis, the EdH torque was created by a driving field along the y axis; while the cross-product torque driving field was applied along the z direction.

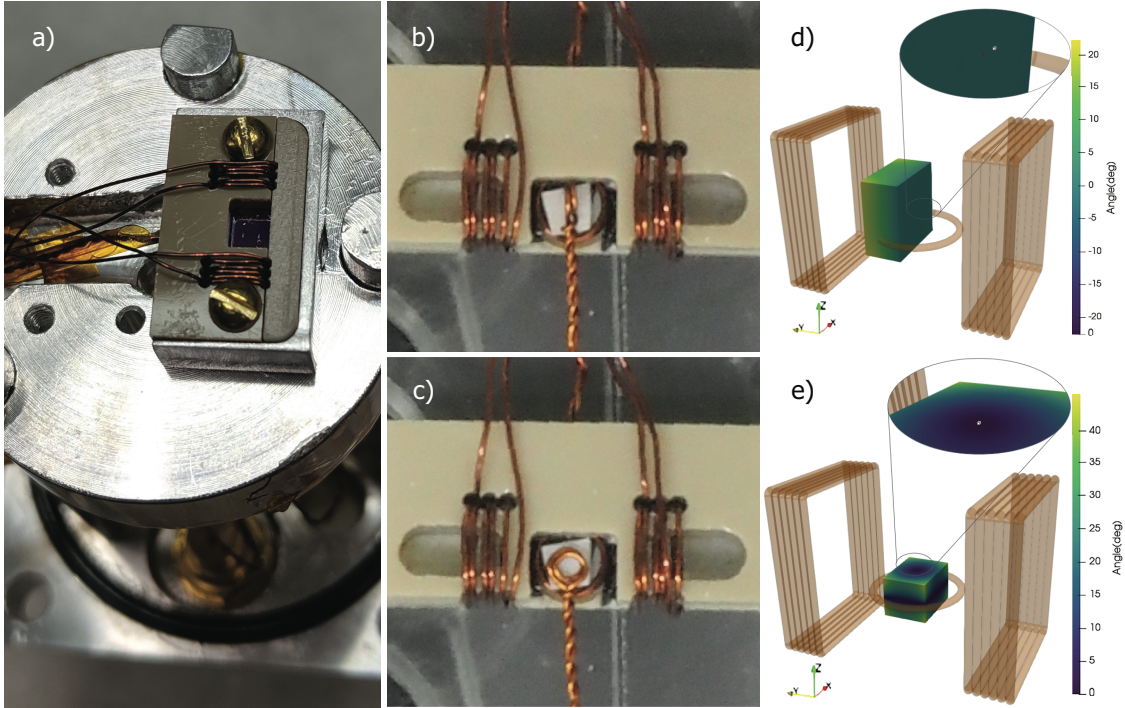


Figure 2.5: Panel a) shows the PEEK assembly on the vacuum stage. Panel b) and c) show sniffer coil orientations for measurement of relative inductive field strengths for y and z respectively. d) and e) show COMSOL simulated field angle deviations from the y and z directions. The white cube at the centre of the field deviation surface plot is roughly representative of the sample size; thus confirming the uniformity of the field over the volume of the sample. Figure used with permission from [33].

To prevent the combination of cross-product and EdH torques we must take care to not produce an admixture of driving field, which has historically been difficult [10]. The fields should also be highly uniform at the location of the sample to reduce effects of magnetic field gradients that could drive magnetic forces and to prevent Lorentz forces due to stray charge on the paddle structure. In addition, the drive field ratio, $\frac{H_y^{\text{RF}}}{H_z^{\text{RF}}}$ is required for calculation of the magnetomechanical ratio, g' . For this reason, a coil form is designed that will ensure that there are highly uniform magnetic fields at the sample location.

The coil form was designed in Autodesk Inventor, and cut out with a CNC wood-working mill. The material chosen for this coil form is polyether ether ketone (PEEK), which is ideal for this application since it is vacuum compatible and electrically insu-

lating. PEEK is also reasonably soft so it can be cut easily in a woodworking mill; PEEK is still structurally strong enough to rigidly hold the sample chip. The coil form (fully assembled: Figure 2.5 panels a)-c)) consists of sections that form a rectangular Helmholtz-like coil, which introduces an alternating field along the y direction. A current loop that is placed directly below the sample chip introduces the RF z field. Both y and z RF driving coils were wound with 30-gauge insulated magnet wire. The H_y^{RF} coils are 4.7 mm wide and 4.9 mm in height, the innermost turns are 3 mm from the sample location, and the coil stack is about 2 mm in width. The H_z^{RF} consists of two turns of 3.2 mm diameter, the sample is about 0.8 mm above the top of the coils.

The ratio of the field can be found in two ways, the first is through an inductive coupling to a coil that can be positioned in three dimensions and rotated 90° to switch between sensing H_y^{RF} and H_z^{RF} . This process is shown in panels b) and c) of figure 2.5. The second method used to find the field ratio is with measurement of current through the coils. This measurement is performed with a Tektronix CT-6 current probe and the signal is monitored on an oscilloscope. In this case, the current is read and the ratio of y to z currents is $\frac{I_y^{\text{RF}}}{I_z^{\text{RF}}} = 1.12 \pm 0.05$. The currents that are measured here can be used as input parameters in COMSOL's AC/DC module to calculate H_y^{RF} and H_z^{RF} via finite element solution of Ampere's law. At the sample location the field ratio yields

$$\frac{H_y^{\text{RF}}}{H_z^{\text{RF}}} = 1.41 \pm 0.05. \quad (2.3)$$

COMSOL simulations yield field strengths across a defined simulation volume, so we can map the uniformity of the field over the sample location. Panels d) and e) show the angular deviation from a pure y and z field respectively; the small white cube represents the sample location. Clearly, the region the sample inhabits is very small compared to the gradient area and we can assume that over the torsional resonator, the magnetic field is uniform.

Subsequent extensions of EdH experiments to smaller scales and even higher frequencies (described in more detail in Chapter 3) will need to rely on magneto-optical

measurement of current [37], a method that is accurate for driving currents at frequencies in excess of tens of GHz. I would like to mention here that the ratio of field strengths is likely the most significant contribution to uncertainty in the calculation for g' and can be vastly improved by magneto-optical RF field measurement.

Field Phase Measurements

We will now direct our attention to another crucially important matter, the measurement of field phase. We wish to obtain a field handedness that is required for determination of drive and field phases of the torque signals. This measurement determines whether the Einstein-de Haas torque phase is in advance, or lags the cross-product torque phase. This measurement can be performed through the previously described inductive measurement of relative field strength via Hall probe. A positive DC current was passed through each field and we measured the current induced by the magnetostatic field. The probe was rotated at such an angle to sense H_z to a position where H_y was measured. The pick-up coil was rotated clockwise and the field magnitude was measured through a Hall probe. An overall sign change of the detected field magnitude indicates that the the field geometry is left handed. In the case of no phase shift, then the field geometry is right handed. In the case of this experiment the field was found to be right handed. This result has bearing on whether or not a torque should be negative or not, an important distinction to be made since phases play a central role in distinguishing EdH torques from conventional cross product torques.

2.2.5 Mechanical resonances of torsional resonators and degree of torsionality (DoT) calculation

COMSOL Multiphysics [35] simulations yield deformational eigenmodes and associated frequencies of nanomechanical resonators; the result of one such simulation is shown in figure 2.1 where an admixture of in-plane rotational and out-of-plane translational behaviour is observed. This combination of twist and flex is related to the

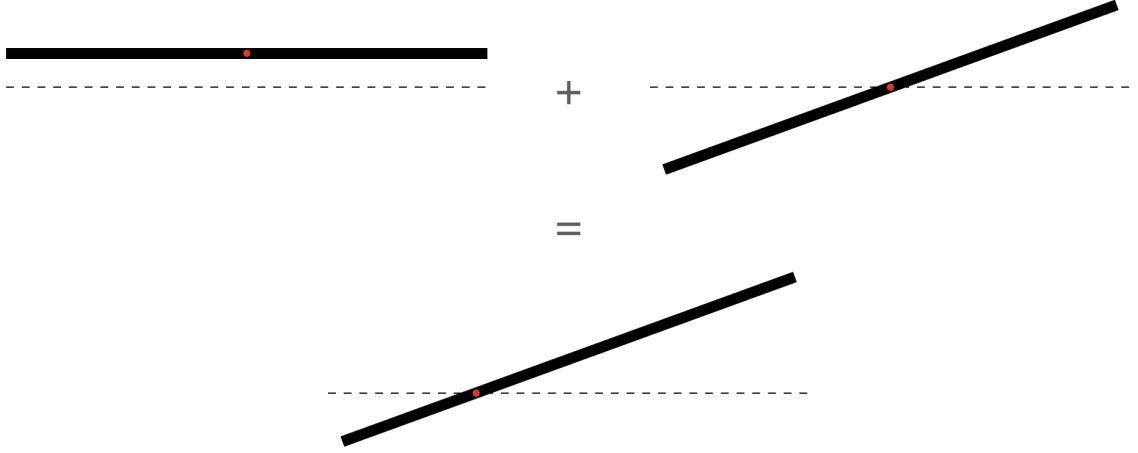


Figure 2.6: A torsional eigenmode that is rotating about an axis that is not the centre of the paddle can be thought of as an addition of a pure translational displacement, and a purely torsional displacement.

proximity of a translational mode to the torsional mode in frequency space and the asymmetric distribution of mass about the torsion axis generated by the mesoscopic YIG disk. To characterize the effectiveness of a mechanical eigenmode's effective sensitivity to torque about a particular axis, we define the degree of torsionality (DoT, $0 \leq \text{DoT} \leq 1$) figure of merit. A perfectly torsional motion results in $\text{DoT}=1$, while a perfectly translational motion yields $\text{DoT}=0$. Figure 2.6 shows how one may consider a rotation about an axis that is displaced from the centre of the torsion paddle, as an admixture of purely translational and torsional modes. By using this linear admixture, we can write the energy equation in the following way where the total velocity v is given by the addition of torsional (rotational) velocity component, v_R , and translational velocity, v_T :

$$E_{\text{Total}} = \iiint \rho v_{\text{Total}}^2 dV = \iiint \rho v_R^2 dV + \iiint \rho v_T^2 dV + 2 \iiint \rho v_R v_T dV \quad (2.4)$$

The above equation can be solved within COMSOL Multiphysics for rotations about various axes, and the ratio of the calculated rotational energy to the total energy gives the DoT ($\text{DoT} = \frac{E_R}{E_{\text{total}}}$). The cross term that contains both velocity terms is generally small compared to the other terms and can be neglected. There are several important steps to consider when calculating the DoT for three axes of torque. For a

f (MHz)	DoT $_x$	DoT $_y$	DoT $_z$
3.577	0.12	0.705	0.0098

Table 2.1: DoT values indicating relative susceptibility to torque drives about each axis for the resonator shown in Figure 2.1

torque along the y direction, torsional motion will be about this axis, so $v_{y,R} = 0$ at any time. In the case of no admixture, we would expect the axis of rotation to pass directly through the centre of the paddle as in the second term on the left hand side of the visual equation in Figure 2.6. Therefore, to decouple translational motion from torsional motion, a subtraction is made along the y axis that shifts the axis of rotation from the centre of mass to the centre of the paddle. Similarly, we can perform the same action for other axes of torque (x and z) wherein the degree of torsionality can tell us about mechanical susceptibility to torque in any three dimensions by adjusting the axis of rotation accordingly. The results for the DoT calculation for each axis of torsional drive are displayed in Table 2.1. Clearly, since DoT $_y$ is the largest, the mechanical eigenmode displayed in Figure 2.1 is most susceptible to torque applied along the y direction. However, due to significant translational motion, DoT $_y \neq 1$.

2.2.6 Toy Model of Coupled Torsional and Translational Modes

Experimental evidence and COMSOL simulations corroborate the frequency propinquity of torsional and translational resonance modes, which could lead to a coupled mechanical motion. This coupling can be recognized as two separate mechanical motions that are simultaneously excited by a torsional drive. It is useful in this case to consider a toy model of two coupled spring systems. A schematic of the spring system is shown in panel a) of Figure 2.7. The system includes a driven torsion spring with torsional spring constant κ , moment of inertia, I , damping constant γ_T , and driving torque τ_D . The torsion spring is coupled to a linear spring that has spring constant k , effective mass m and damping constant γ_L . The torsion and linear springs are

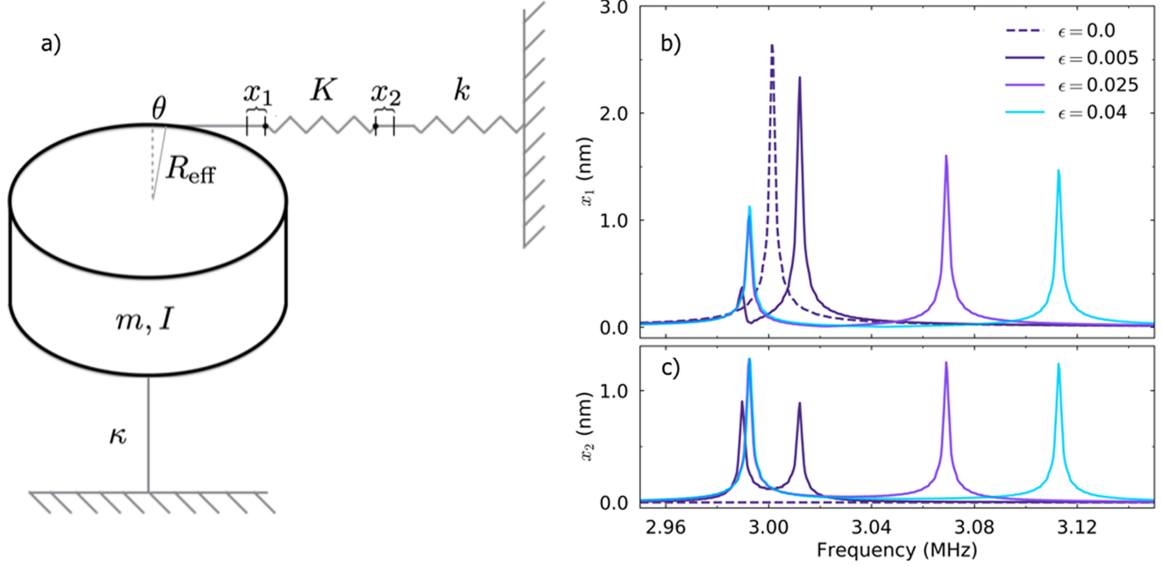


Figure 2.7: A toy model of coupled resonances is illustrated in panel a) where a torsional spring with spring constant κ is coupled to a linear spring with spring constant k through a third spring with spring constant $K = \epsilon k$. The displacement from equilibrium position is represented by $x_1 \approx R_{\text{eff}}\theta$ and x_2 . Panel b) and c) represent solutions to Equation 2.6 for various driven frequencies. Measurements of displacements represent deflections of each spring due to some stimulus of a driving torque. Figure used with permission from [33].

coupled by a third spring with spring constant $K = \epsilon k$. By utilizing similar methods found above for DoT calculation, COMSOL simulations also may yield values for κ and I for the torsional resonator since for small angular deviations from equilibrium,

$$\kappa = (2\pi f_{\text{mech}})^2 I = (2\pi f_{\text{mech}})^2 \iiint \rho(x, y, z) \|\vec{r}\|^2 dV \quad (2.5)$$

where $\rho(x, y, z)$ is the mass density of the resonator and \vec{r} is a vector in the plane of rotation. The moment of inertia for the device shown in Figure 2.1 is $I = 4.78 \times 10^{-26}$ kg m² and the torsion spring constant is $\kappa = 1.7 \times 10^{-13}$ Nm.

We can reframe the nanomechanical torsional resonator's motion as a system of coupled differential equations that represent the motion of our toy model spring system

$$\begin{aligned} \frac{I}{R_{\text{eff}}} \frac{d^2 x_1}{dt^2} &= -\left(\frac{\kappa}{R_{\text{eff}}} + K R_{\text{eff}}\right) x_1 + K R_{\text{eff}} x_2 - \frac{\gamma_T}{R_{\text{eff}}} \frac{dx_1}{dt} + \tau_D \cos(\omega t) \\ m \frac{d^2 x_2}{dt^2} &= -(k + K) x_2 - \gamma_L \frac{dx_2}{dt} + K x_1. \end{aligned} \quad (2.6)$$

The solution to this system of coupled differential equations will tell us the displacement response of the resonator as a result of applying a sinusoidally varying, purely torsional drive at a frequency ω . We represent the displacement from the equilibrium position of the torsion spring as x_1 , and by the small angle approximation we may write $x_1 \approx R_{\text{eff}}\theta$; the displacement from equilibrium of the linear spring is given by x_2 . The above system of second order differential equations can be reduced to a system of first order coupled differential equations by a judicious change of variable wherein the initial conditions are encoded. Here we introduce variables y_1 and y_2 where $y_1 = \frac{dx_1}{dt}$, and $y_2 = \frac{dx_2}{dt}$. The above system of equations becomes a system of four first order differential equations

$$\begin{aligned}
y_1 &= \frac{dx_1}{dt} \\
\frac{I}{R_{\text{eff}}} \frac{dy_1}{dt} &= -\left(\frac{\kappa}{R_{\text{eff}}} + KR_{\text{eff}}\right)x_1 + KR_{\text{eff}}x_2 - \frac{\gamma_T}{R_{\text{eff}}}y_1 + \tau_D \cos(\omega t) \\
y_2 &= \frac{dx_2}{dt} \\
m \frac{dy_2}{dt} &= -(k + K)x_2 - \gamma_L y_2 K x_1
\end{aligned} \tag{2.7}$$

Equation 2.7 can be solved using numerical integration in python (details of this code are presented in Appendix B). The solution finds the magnitude of displacement of the torsional spring, x_1 , and coupled linear spring, x_2 . Reflecting experimental data, the driving frequency is swept and solutions for each applied frequency were compiled. The magnitude of the displacements are recorded and plotted in figure 2.7 panels b) and c) for various coupling strengths. The case of $\epsilon = 0$ yielded no coupling between the driven torsion spring and linear responding spring. As the coupling increases, a second resonance displacement emerged in x_2 . This mode grows in relative magnitude until, at $\epsilon = 0.04$, the torsional and translational motion are equivalent.

We found that a coupling parameter $\epsilon = 0.025$ reflected the experiment well since the torsional mode was found about 5% higher in frequency than the translational mode. Additionally, displacement profiles found in raster scan data reflect similar relative amplitudes of displacement when acted on by a torsional drive.

2.2.7 Thermomechanical Torque Calibration

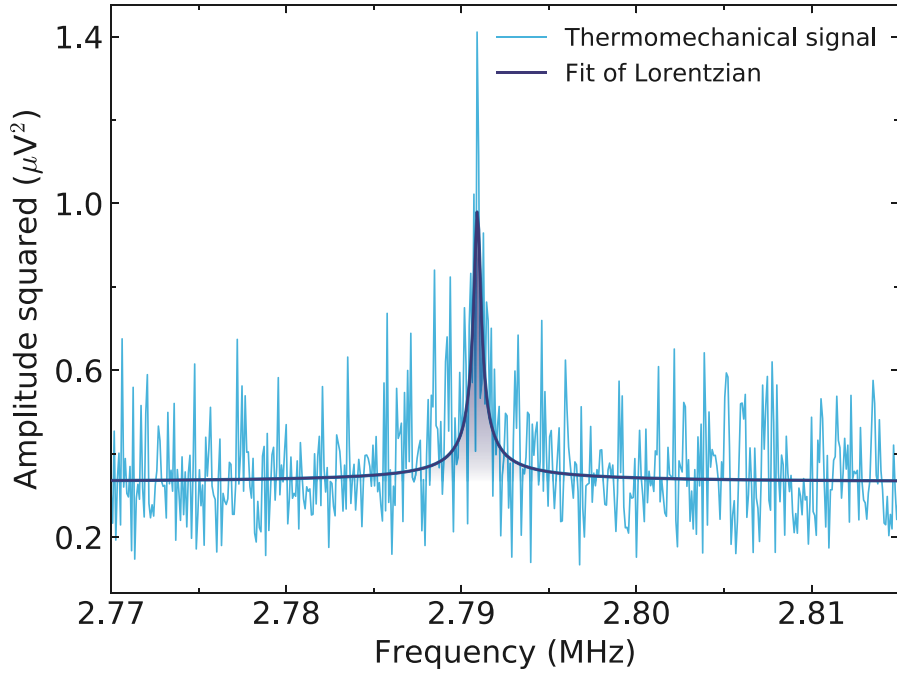


Figure 2.8: A squared fit to the response of an undriven thermomechanical frequency sweep measured with a 46 Hz noise equivalent power bandwidth. The resonant frequency is $f_0 = 2.79092 \pm 0.00007$ MHz, and the mechanical resonance quality factor is $Q = 1300 \pm 300$. Figure used with permission from [33].

So far we have used an external driving field to excite torsional mechanical resonances, however measurement of driven signals does not provide a sense of the true mechanical torque exerted on the resonator by EdH or cross-product torques. This is a consequence of our detection technique which, converts optical power into an AC electrical signal at the photoreceiver location, and is then input to a lock-in amplifier. Therefore, the signal magnitude is represented in units of V. In reality, the interferometric modulation is a measurement of the resonator paddle displacement. Conversion of the electrical signal to a value of torque in Nm can be performed through thermomechanical calibration.

For a sufficiently low experimental background noise floor we may drive mechanical resonances of our devices with Brownian motion. The fluctuation-dissipation theorem

permits study of a system at its equilibrium state without imposing an external force on the system that would otherwise drive the system out of thermal equilibrium. When no torque is imparted upon the mechanical resonator by the magnetic specimen, equilibrium fluctuations couple to the mechanical resonator. In other words: the Brownian motion of atoms in the resonator acts as a broadband, phase-independent source of mechanical excitation. Thermal excitation yields a calibration constant that may convert a lock-in amplifier or spectrum analyzer signal into units of mechanical torque. Thermomechanical calibration techniques have been studied in a variety of systems from torsional resonators [38], to nanobeams [39], and a general process for thermally driven mechanical displacements has been reported [40].

We will begin our calculation of the thermomechanical calibration constant by writing the energy of a torsional spring. We approximate that the energy of a torsion spring is equivalent to the energy of our torsional eigenmode

$$E_{i,\text{rot}} = \frac{1}{2} \kappa_i^{\text{eff}} \langle \theta_i^2 \rangle. \quad (2.8)$$

κ_i^{eff} is the effective torsional spring constant for torsion axis i (kept arbitrary for the purposes of this discussion), and $\langle \theta_i^2 \rangle$ is the average angle squared for an induced torque along the axis $i = (x, y, z)$. Utilizing the harmonic relation between angular frequency, moment of inertia and the effective spring constant, we can use finite element analysis software (COMSOL) once again to obtain the parameters I_i and κ_i as described in 2.2.5.

The equipartition of energy is set equal to the rotational energy for some temperature, T , since the broadband thermal drive favours no particular system axis,

$$\langle \theta_i^2 \rangle = \frac{k_b T}{\kappa_i^{\text{eff}}} \quad (2.9)$$

where k_b is Boltzmann's constant. The above yields $\langle \theta_i^2 \rangle = 23.95 \times 10^{-9} \text{ rad}^2$. Under the assumption of small angles, we may modify the above equation to give the mean displacement by utilizing the distance from the axis of torque to the location of interferometric detection $\langle x_i^2 \rangle \sim R_i^2 \langle \theta_i^2 \rangle$. For our device $R_i = 5.17 \times 10^{-7} \text{ m}$ which gives

an average square displacement of $\langle x_i^2 \rangle = 6.402 \times 10^{-21} \text{ m}^2$. The mechanical response of such a thermal drive is described by a Lorentzian, from which the frequency-dependent angular spectral density, $S_{\theta_i}(f)$, can be obtained in units of rad^2/Hz for a mechanical device with torsional eigenfrequency f_i and resonance quality factor Q_i

$$S_{\theta_i\theta_i}(f) = \frac{2k_b T f_i^3}{\pi \kappa_i^{\text{eff}} Q_i} \frac{1}{(f_i^2 - f_0^2)^2 + (\frac{f_0 f_i}{Q_i})^2}. \quad (2.10)$$

By taking the peak spectral density (S_{x_i} is maximized for $f_i = f_0$) and multiplying by R_i^2 we find

$$S_{x_i x_i} = \frac{2Q_i \langle x_i^2 \rangle}{\pi f_0}. \quad (2.11)$$

The displacement square spectral density is $S_{x_i x_i} = (1.9 \pm 0.4) \times 10^{24} \text{ m}^2/\text{Hz}$. Using this equation we can find the torque spectral density where a factor of Q_i^{-1} is included to reflect the enhancement of the torque at mechanical resonance

$$S_{\tau_i} = \frac{\kappa_i^{\text{eff}} \sqrt{S_{x_i x_i}}}{R_i Q_i}. \quad (2.12)$$

With the equations that have been presented so far, we find a torque spectral density value of $S_{\tau_i} = 0.11 \pm 0.02 \text{ zNm}/\sqrt{\text{Hz}}$.

Now that the mechanical spectral density has been obtained, we must perform an analysis to find the voltage spectral density due to our detection equipment $S_{V_i V_i}$. This can simply be found from the square of the peak height, $V_{i,\text{peak}}$, subtracted from the height of the noise floor, $V_{i,\text{background}}$, divided by the bandwidth of the lock-in measurement, f_{BW}

$$S_{V_i V_i} = \frac{V_{i,\text{peak}}^2 - V_{i,\text{background}}^2}{f_{\text{BW}}}. \quad (2.13)$$

From the peak and background of the fit shown in Figure 2.8 we find $S_{V_i} = 0.110 \text{ } \mu\text{V}/\sqrt{\text{Hz}}$.

To obtain the calibration factor, \mathcal{C}_{τ_i} , we divide the torque spectral density by the voltage spectral density, resulting in a conversion factor in units of Nm/V . For the device used in the present work, we find $\mathcal{C}_{\tau_i} = 1.0 \pm 0.2 \text{ aNm}/\text{mV}$. A driven, calibrated resonance is displayed in figure 2.9.

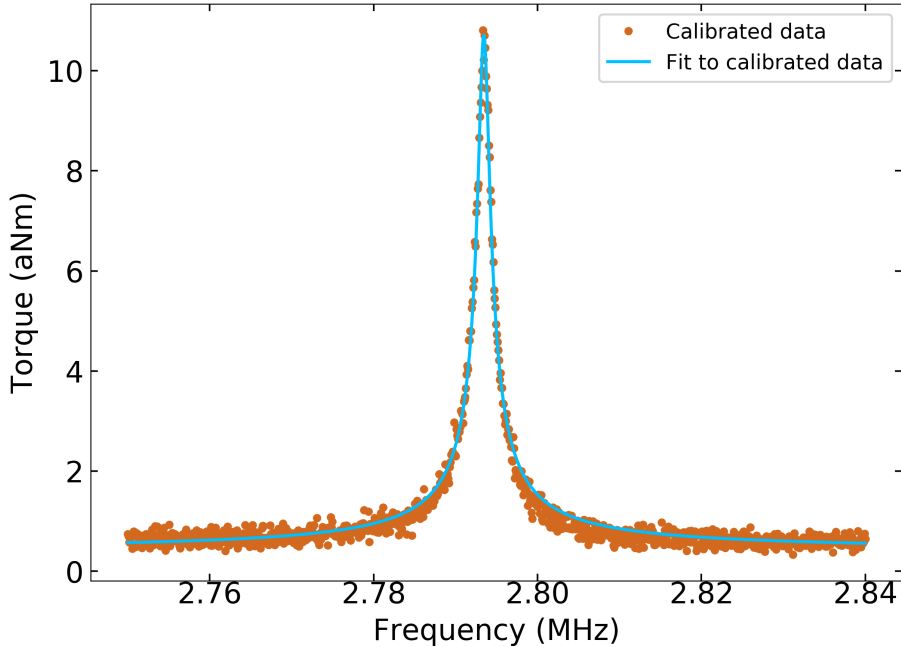


Figure 2.9: Calibrated fit to a driven cross product torque signal. The resonant frequency is 2.793452 ± 0.000008 MHz, the quality factor, Q , of the resonance is 1930 ± 20 . Just two standard deviations different from the value obtained in the thermomechanically driven signal.

2.3 Experimental Results and Calculation of the Magnetomechanical Ratio g'

Now that a description of the experimental apparatus and calibration methods is complete, we will study the results of our simultaneous measurements of EdH and cross-product torques generated by mesoscopic YIG disks. Keeping with the historical tradition of Einstein-de Haas torque experiments, the magnetomechanical ratio g' was calculated. This calculation marks the first measurement of its kind for YIG. A key feature of this experiment is the ability to observe similar magnitudes of cross-product and EdH torques simultaneously; this feature enables the calculation of g' as discussed in 2.3.3.

To calculate the magnetomechanical ratio we will take advantage of the field where the ratio of EdH and cross-product torques is unity. Let us briefly dive into the derivation for the calculation of g' . As we know from Section 1.3 conventional cross

product torques are magnetic torques generated by a field, \vec{H} , acting on a magnetic moment, \vec{m} . We find $\vec{\tau}^{m \times B} = \mu_0 \vec{m} \times \vec{H}$. Based on our mechanical geometry we are interested in torque about the y axis. By writing the y component of torque we find

$$\tau_y^{m \times B} = \mu_0 (m_z H_x^{\text{DC}} - m_x H_z^{\text{RF}} \sin(\omega t)). \quad (2.14)$$

We make substitutions for the magnetic moment terms by relating magnetic moment to magnetization and to the field using the magnetic susceptibility χ ($\vec{m} = V \vec{M} = V \chi \vec{H}$). Expanding the field term, we find $\vec{H} = \vec{H}_{\text{external}} + \vec{H}_{\text{demag}}$. For a particular coordinate of field, $H_{i,\text{demag}} = N_i H_{i,\text{external}}$, where N_i is the demagnetization factor such that $\sum_i N_i = 1$. In the case of our three-dimensional mesoscopic YIG disks, we assume two demagnetization factor terms: the radial factor, N_r , which represents demagnetization for all directions in-plane due to cylindrical symmetry, and the out-of-plane factor, N_z . N_r can be rewritten in terms of N_z : $N_r = \frac{1-N_z}{2}$. We arrive at the following equation for the cross product torque along the y axis

$$\tau_y = (\chi V (1 - N_z) H_z^{\text{RF}} \sin(\omega t)) \mu_0 H_x^{\text{DC}} - (\chi V (1 - N_r) H_x^{\text{DC}}) (\mu_0 H_z^{\text{RF}} \sin(\omega t)), \quad (2.15)$$

which is further simplified to

$$\tau_z^{m \times B} = -\mu_0 (N_z - N_r) \chi V H_x^{\text{DC}} H_z^{\text{RF}} \sin(\omega t). \quad (2.16)$$

We may use a similar substitution for m to obtain the RF EdH torque. The angular momentum along y , J_y is given in the following way

$$J_y = \frac{2m_e}{eg'} m_y = \frac{2m_e}{eg'} \chi V (1 - N_r) H_y^{\text{RF}} \sin(\omega t). \quad (2.17)$$

To find the EdH torque, we calculate the time rate of change of the angular momentum (Equation 2.1)

$$\tau_y^{\text{EdH}} = -\frac{dJ_y}{dt} = -\frac{2m_e}{eg'} \chi V (1 - N_r) \omega H_y^{\text{RF}} \cos(\omega t). \quad (2.18)$$

Conveniently, simultaneous measurement of EdH and cross-product torques allow us to take the ratio of the two torques at a precise static field strength and drive

frequency. By substituting $\gamma' = \frac{g'e}{2m_e}$ and $c_\tau = \frac{1-3N_r}{1-N_r}$ we obtain the ratio of the torques as determined in Equations 2.16 and 2.18

$$\frac{\tau_y^{m \times B}}{\tau_y^{\text{EdH}}} = \frac{\mu_0 c_\tau \gamma' H_x^{\text{DC}} H_z^{\text{RF}}}{2\pi f H_y^{\text{RF}}}. \quad (2.19)$$

As a consequence of the frequency scaling of EdH torques, we suspect that EdH torques will be of similar magnitude to cross-product torques. It follows that in a simultaneous measurement where the DC field was swept while the frequency was held constant, we will find a point where the cross-product and EdH torque signals are equivalent. At this static field strength, the ratio of EdH and cross-product torques becomes unity, and we can recast H_x^{DC} as $H_x^{\text{Crossover}}$

$$1 = \frac{\mu_0 c_\tau \gamma' H_x^{\text{Crossover}} H_z^{\text{RF}}}{2\pi f H_y^{\text{RF}}}. \quad (2.20)$$

By solving for g' we arrive at

$$g' = \frac{4\pi m_e}{\mu_0 e c_\tau} \frac{f}{H_x^{\text{Crossover}}} \frac{H_y^{\text{RF}}}{H_z^{\text{RF}}}. \quad (2.21)$$

The above equation contains all the necessary information required to find the magnetomechanical ratio g' . In addition to the physical constants, we already have found the relative field strength ratio in Section 2.2.4. We will see in Section 2.3.1 that c_τ can be found by using micromagnetic simulation software and high field hysteresis loops of cross-product torques as a sensitive probe of the magnetic volume aspect ratio. Additionally, we will see in Section 2.3.3 that $H_x^{\text{Crossover}}$ and f are found by way of simultaneous measurement of EdH and cross-product torque over a range of low DC bias field.

2.3.1 Characterization of Mesoscopic YIG Disk Active Magnetic Volume

One of the consequences of miniaturizing Einstein-de Haas experiments on mesoscopic YIG disks is the manifestation of a magnetically inactive layer that forms when ion milling is used to cut disks to be mounted on torsional resonators, as described in

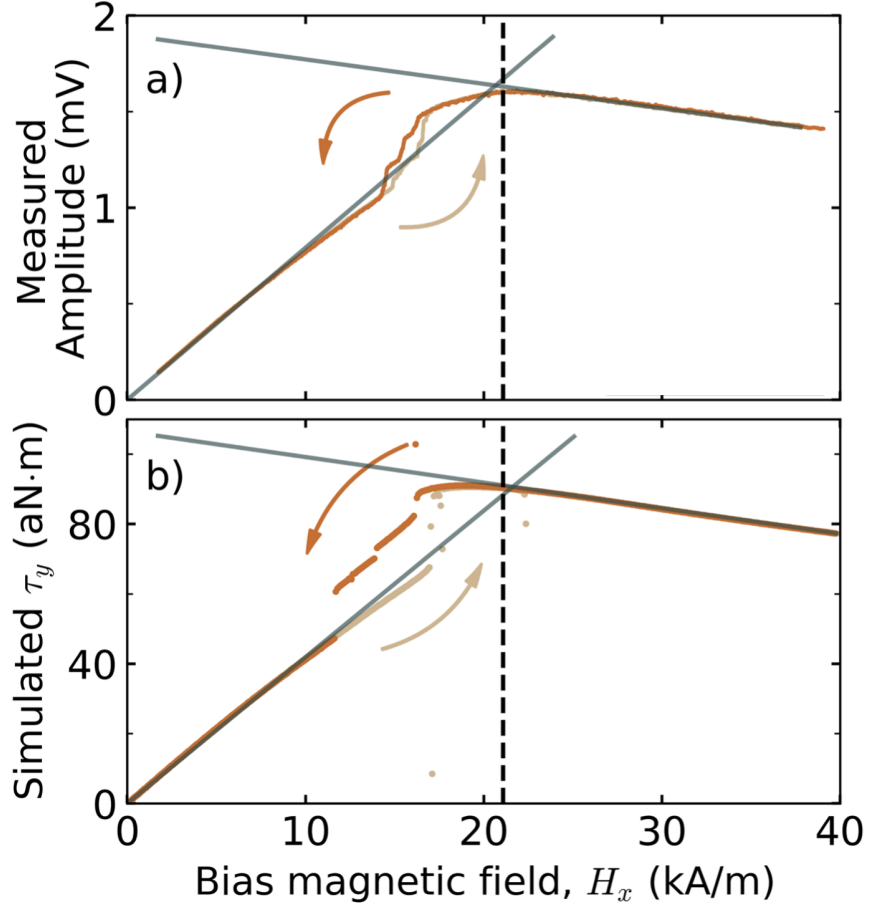


Figure 2.10: Experimental (panel a) and simulated (panel b) hysteresis loops generated by the cross-product torque from the YIG disk. Two linear fits are applied to the each hysteresis curve: one to the low field vortex regime, the other to the high field quasi-static regime. The intersection of these curves (indicated by the dashed line) is a sensitive probe of magnetic aspect ratio.

subsection 2.2.1. This introduces an uncertainty in the dimension of YIG disks. We introduce a method for obtaining magnetic aspect ratios of a YIG disk through cross-product torque hysteresis loops.

Micromagnetic demagnetizing factors are central to obtaining a value for c_τ and, in turn, the magnetomechanical ratio, g' . As described in Section 2.2.1, the Ga bombardment of the YIG/GGG/YIG wafer, created a magnetically inactive layer due to Ga implantation. The magnetically inactive layer introduces significant uncertainty in the true magnetic volume and shape of the YIG, which is essential for our calculation of g' . While the shape of the disk is cylindrical, the magnetic volume geometry is

unknown. We assumed two cases for the magnetic volume: cylindrical, or ellipsoidal. The axial demagnetizing factor of an axially symmetric ferromagnet can be found in the following two ways, the first, reported by Beleggia et al. [29] wherein the magnetic specimen is approximated as an ellipsoid, the second solution by Joseph et al. [28] is for a cylindrical ferromagnet. For the case of a prolate or oblate axially symmetric ellipsoid of height h and diameter d in terms of the aspect ratio, $\alpha = \frac{h}{d}$, Beleggia writes

$$\begin{aligned} N_r^{\text{oblate}} &= 1 - \frac{2}{\epsilon^2} \left(1 - \frac{\sqrt{1-\epsilon^2}}{\epsilon} \arcsin(\epsilon) \right), & \epsilon &= \sqrt{1-\alpha^2}, (\alpha \leq 1) \\ N_r^{\text{prolate}} &= 1 - \frac{2(1-E^2)}{E^2} \left(\frac{1}{2E} \ln \left(\frac{1+E}{1-E} \right) - 1 \right), & E &= \sqrt{1-\frac{1}{\alpha^2}}, (\alpha \geq 1). \end{aligned} \quad (2.22)$$

The solution for the demagnetizing factor of a cylinder is given in terms of $K(k)$ and $E(k)$, the complete elliptic integrals of first and second kind. The demagnetizing factor is

$$N_r = 2 \left(\frac{\alpha E(k)}{\pi k} - \frac{\alpha k K(k)}{4\pi} (4 + \alpha^2) + \frac{1}{2} \right). \quad (2.23)$$

The above equations grant us a crucial piece of intuition: as the aspect ratio of a disk or ellipsoid decreases, N_r becomes large. This relationship indicates that it is easier to magnetize a ferromagnetic ellipsoid along radial directions due to a weakened demagnetizing field.

As a ferromagnet becomes easier to magnetize, it will more easily saturate in the presence of an external field. Ferromagnetic saturation is indicated by the spin texture transition out of the demagnetized ground state in low field, to the quasi-uniform state in higher field. The quasi-uniform spin texture is clearly distinguished from other possible spin textures due to its monotonic decrease in magnetic torque magnitude. As a result we can use the vortex spin texture annihilation as a probe of aspect ratio. In panel a) of Figure 2.10, a high field hysteresis loop is shown where cross-product torque was measured. The YIG was in the vortex spin texture in the low field, as indicated by the linear increase in signal and positive slope. Vortex annihilation occurs in intermediate field before entering the quasi-uniform spin texture

state beyond saturation, where the torque signal decreases as the field increases. In these two regimes, the demagnetizing factors are intimately related to the torque rate of change with DC bias field. The micromagnetic vortex is a significantly in-plane demagnetized spin texture, so the disk will magnetize more easily for a larger aspect ratio. This susceptibility results in a positive slope that was observed as DC field increases. We can similarly consider the linear increase of torque in the vortex state via the spin texture. The vortex core is less susceptible to movement in plane for a smaller diameter (while maintaining a similar disk height) so the slope will be greater. In the high-field quasi-uniform spin texture regime N_z is dominant since the monotonic decrease in torque is due to the reduced effect of dither field compared to DC bias field. Equation 1.6 shows that the AC torque is directly proportional to the angle created between H^{DC} and H^{AC} , as the bias field increases, this angle decreases.

The relationship between bias field strength and linear increase of torque at low field and linear decrease of torque at high field act in concert to produce a sensitive probe of magnetically active volume aspect ratio. We compared experimental results to mumax3 [31] micromagnetic simulations of cross-product torque hysteresis loops. By applying a linear fit to the low field, and high field regimes, an intersection point of the two lines was found. Subsequent micromagnetic torque hysteresis loops were run for comparison while the aspect ratio was adjusted. A simulated hysteresis loop is displayed in Figure 2.10 panel b) where intersection points were found at an applied field magnitude of 21 kA/m. The simulation in panel b) is the result of a cylinder with a diameter of 2.0 μm and 0.46 μm thickness, which yielded an aspect ratio of $\alpha = 0.23 \pm 0.01$. The uncertainty was bracketed by additional simulations where the aspect ratio was adjusted slightly. Using equation 2.23 the result for the out-of-plane demagnetization factor was found to be $N_z = 0.72 \pm 0.02$, thus $N_r = 0.14 \pm 0.01$, and $c_\tau = 0.88 \pm 0.03$.

The simulation-verified magnetic volume aspect ratio adds yet another crucial piece of information to our calculation of g' , that is the demagnetizing factors N_r and N_z

that in turn yield c_τ . In the next Section we will discuss simultaneous measurements of cross-product and EdH torques wherein the crossover field, $H_x^{\text{Crossover}}$, was found and the magnetomechanical ratio for YIG is calculated.

2.3.2 Frequency Dependent Measurement of EdH and Cross Product Torques

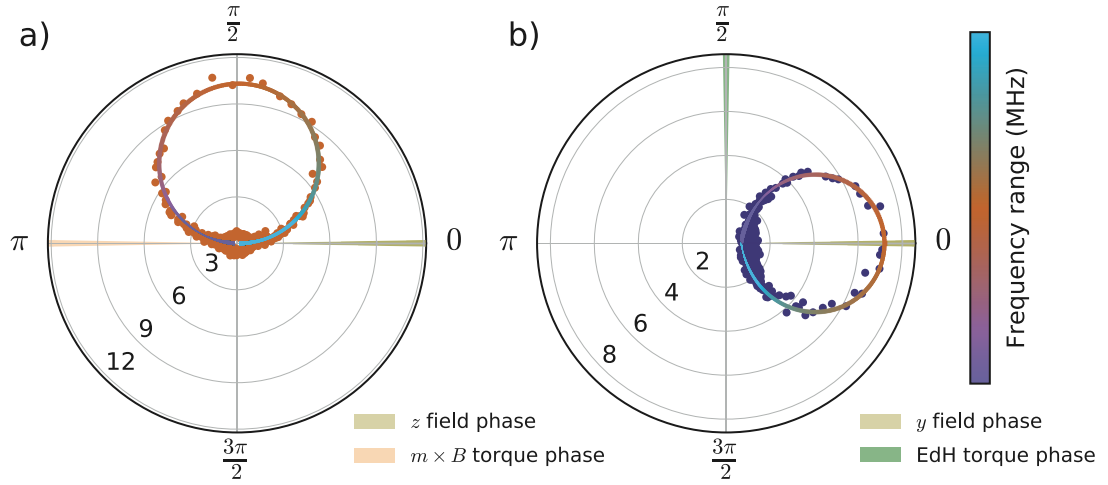


Figure 2.11: Polar plots of frequency sweeps. The frequency here was swept from 2.75 MHz to 2.84 MHz. The mechanical resonance due to a driving cross-product torque is shown in panel a) and the mechanical resonance due to a driving EdH torque in panel b). The two resonances are, when $\omega = \omega_0$, out of phase by 90° with one another. The true torque phase is given by the orange and green rays for cross-product and EdH torques respectively. The width of the rays represents the uncertainty in phase at the resonance maximum.

To simultaneously measure cross-product and EdH torques, we ensure that each torque is distinct in phase as outlined in Section 2.1. The phase of each torque is the essential quality that allows us to distinguish EdH from cross-product torque. Equation 2.18 indicates that EdH torques exhibit a 90° phase shift relative to the driving field, while Equation 2.16 shows that cross-product torques are in-phase with the driving field. Cross-product torques scale in magnitude linearly with increasing DC bias field while EdH torques are bias field independent. Enabled by RF lock-in detection, our measurements are sensitive to both amplitude and phase.

To draw a clear distinction between the phase of EdH and cross-product torque signal, we present the resonance signature in polar coordinates along with expected drive and torque phases. A driven, damped oscillator at resonance has the following frequency dependent amplitude, $A(\omega; \omega_0, Q, a)$

$$A(\omega; \omega_0, Q, a) = \frac{a^2}{\sqrt{(\omega_0^2 - \omega^2)^2 + \frac{\omega_0^2 \omega^2}{Q^2}}}, \quad (2.24)$$

with a scaling factor a , resonant frequency ω_0 , driving frequency ω , and resonant quality factor Q . The resulting frequency dependent phase, $\phi(\omega; \omega_0, Q)$ is

$$\phi(\omega; \omega_0, Q, \phi_0) = \arctan\left(\frac{\omega_0 \omega}{Q(\omega_0^2 - \omega^2)}\right) + \phi_0. \quad (2.25)$$

ϕ_0 is a phase offset, which for the purposes of this discussion, includes components of phase delay that are picked up through electronics and optics. We can see here that the phase offset begins at $\phi(0; \omega_0, Q, 0) = 0$, then at resonance $\phi(\omega_0; \omega_0, Q, 0) = \pi/2$, and in the high frequency limit $\phi(\omega \gg \omega_0; \omega_0, Q, 0) = 0$. It is convenient for visualization sake, to present the above equations in polar coordinates. For some drive frequency that is swept through a resonance, a Lorentzian peak emerges in amplitude while there is a 180° phase shift. In polar coordinates, a Lorentzian resonance signature traces a circle with a circumferential terminus at the origin of the polar map. A line that equally bisects this circle passes through the origin and the furthest point on the circle from the origin can be used to determine the amplitude maxima, and if referenced to the 0° ray, gives the phase at the peak amplitude. If we consider two resonant responses separated by 90° of phase, the circles will be identical but will have pivoted about the origin. This is precisely the case in Figure 2.11 for the measured cross-product torque in panel a), and EdH torque in panel b). The frequency was swept through the mechanical resonance. The colourbar represents the lowest frequency of 2.75 MHz (purple) to the highest frequency, 2.84 MHz (light blue). The fit that was applied to this data simultaneously encapsulates the amplitude and phase as a function of frequency. It is convenient to use the in-phase, X , and quadrature,

Y , outputs of a lock-in amplifier to fit the frequency sweeps where

$$\begin{aligned} X(\omega; \omega_0, Q, a) &= A(\omega; \omega_0, Q, a) \cos(\phi(\omega; \omega_0, Q)) \\ Y(\omega; \omega_0, Q, a) &= A(\omega; \omega_0, Q, a) \sin(\phi(\omega; \omega_0, Q)). \end{aligned} \tag{2.26}$$

As can be seen in Figure 2.11 a very distinct phase difference was found between the two signals. In both of these cases, the phase offset introduced by the apparatus and field producing coil was zero (indicated by the beige ray). We anticipated there would be a 90° phase lag at the resonance peak indicated by Equation 2.25 so the true torque phases are indicated by the cross-product (pink) and EdH (green) torque phase rays. The width of the ray indicates the uncertainty in phase at the amplitude maximum. Despite the drastic phase difference, the amplitude of the resonances are of comparable magnitude. We now extend our measurements to simultaneously measured minor hysteresis loops, where the driving frequency was held fixed, and the bias DC field was swept.

2.3.3 Simultaneous Measurement of Cross-product and EdH Torques

We have so far demonstrated the relative phase relationship between the cross-product and EdH torques, which indicated the clear distinction between each torque's origin. We now will focus on results from simultaneous measurements of EdH and cross-product torques that are made possible by the frequency scaling of EdH torques. Simultaneous measurements allow us to exhibit the field-independent behaviour of the EdH torque in stark contrast with the cross-product torque. Simultaneous torque measurements also permit measurement of $H_x^{\text{Crossover}}$, which is the final parameter required to calculate g' for YIG. Both the EdH and cross-product torques are applied along the y axis and the two driving magnetic fields were slightly detuned from the resonant peak by ± 100 Hz. This ensured there was no admixture of the signals and each signal had a sufficiently large signal-to-noise ratio so any small changes in the torques could be captured. To find the the crossover field, the static field was swept

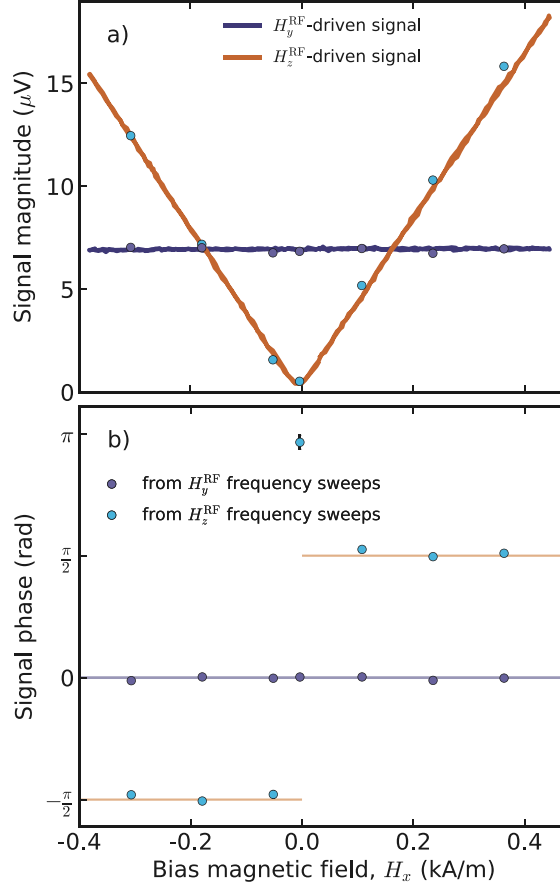


Figure 2.12: Simultaneous measurement of cross-product (driven by H_z^{RF}) and EdH (driven by H_y^{RF}) torques over a range of small bias DC field. The solid lines represent data measured while changing the DC field magnitude. The points represent frequency sweep data at discrete DC field strengths. Discrete frequency sweep measurements offer superior phase SNR than the continuously swept DC field measurement, and therefore are exclusively included in panel b). Panel a) features two intersections of the EdH and cross-product signal that are used to calculate the crossover field, $H_x^{\text{Crossover}}$.

from -0.4 kA/m to 0.4 kA/m. This static field range featured the zero crossing of the cross-product torque and two crossover field points. Figure 2.12 panel a) shows the amplitude of the torques over the field range of the measurement. Owing to the high frequency of these driving fields, the EdH torque magnitude exceeds the cross-product torque in low field. Panel b) of Figure 2.12 shows the phase, where once again there is a 90° phase difference between EdH and cross-product torques. In addition to having a bias magnetic field sweep, several discrete points have been included where a

frequency sweep was performed for an unchanging DC field. Each discrete point is the product of a measurement of simultaneously detected cross-product and EdH torques. The torques, again to avoid admixture of the signals, were driven with a relative frequency separation of 200 Hz. The frequency sweeps were fit with a Lorentzian function that gave resonant frequency f_{mech} , resonant quality factor, Q , and peak amplitude. The resulting magnitude at the appropriate drive frequency was plotted as a point in figure 2.12 panel a), while the phase information was included in panel b). The inclusion of discrete points from independent sweeps of frequency provides a more consistent phase measurement than the field sweep was able to. The relative phase difference from one frequency sweep to the next is 5.7° , while the variation that is observed for field sweeps can be much larger. Unfortunately a phase-locked-loop (PLL) cannot be implemented to improve this measurement since the cross-product torque goes through zero, and reverses phase; under these conditions the loop would fail.

From the data presented in Figure 2.12 we obtained the crossover field, $H_x^{\text{Crossover}}$: the static field strength where the cross-product torque signal intersects the EdH signal. Since there are two points of intersection, the crossover field was taken to be one half the bias field separation between the two crossover points in the negative and positive bias field which gave a crossover field of $H_x^{\text{Crossover}} = 170 \pm 5$ A/m. The crossover field is the final measurement required to measure the magnetomechanical ratio g' . Using equation 2.21, the magnetomechanical ratio is

$$g' = \frac{1}{(1.3 \pm 0.1) \times 10^4 \text{ m/C}} \frac{2.7904 \text{ MHz}}{(170 \pm 5 \text{ A/m})} (1.41 \pm 0.05) \quad (2.27)$$

$$g' = 1.78 \pm 0.16.$$

We anticipate that our value for g' should follow the approximate relation $2 - g' \approx g - 2$. The g-factor, g , for YIG has been reported by Dillon through measurements of ferrimagnetic resonance [41]. Their results yield $g = 2.005 \pm 0.002$. If this relation is accurate, our result for the magnetomechanical ratio is 1.4 standard deviations from our expectation for g' .

Figure 2.12 reveals not only the striking magnitude similarities between the EdH and cross-product torques, but indicates that the EdH torque is, as expected, independent of applied DC field. The RF magnetic fields that drive the two torques are highly uniform, so signal admixture does not limit us to studying torques at small DC fields. In subsequent Sections, we will discuss results from simultaneous torque measurements of EdH and cross-product torques at high fields where the micromagnetic vortex state annihilates, giving way to the quasiuniform spin texture state.

2.3.4 Einstein-de Haas Torques at Larger DC Field Magnitudes and Beyond Vortex Annihilation

The highly uniform driving fields across the sample geometry enabled the extension of EdH experiments into the higher field regime without significant admixture of EdH and cross-product torques. As such, high-field extension will be the topic of the remainder of this chapter. We introduced a 2"×2"×2" neodymium iron boron (NdFeB) cube magnet mounted upon a stepper motor track that was able to translate along the x -axis. A three-axis Hall probe was used to record the field as the cube magnet was translated. The NdFeB magnet permitted extension to much higher field strength capable of saturating the YIG disk. The extension to higher field also allowed for the use of a PLL so high stability measurements of phase changes could be performed.

Simultaneous Measurement of Cross-product and EdH Torques in Vortex Spin Texture

As seen in Figure 2.13 panel a), the cross-product torque rapidly becomes much larger than the EdH torque magnitude owing to the linear DC field dependence of the cross product torque. The EdH torque magnitude, on the other hand, is very flat out to approximately 5 kA/m but then begins to increase. The monotonic decrease in EdH torque phase indicates that an admixture of H_z^{RF} driven signal was introduced to the H_y^{RF} driven signal. As we saw in the previous section, the EdH torque phase

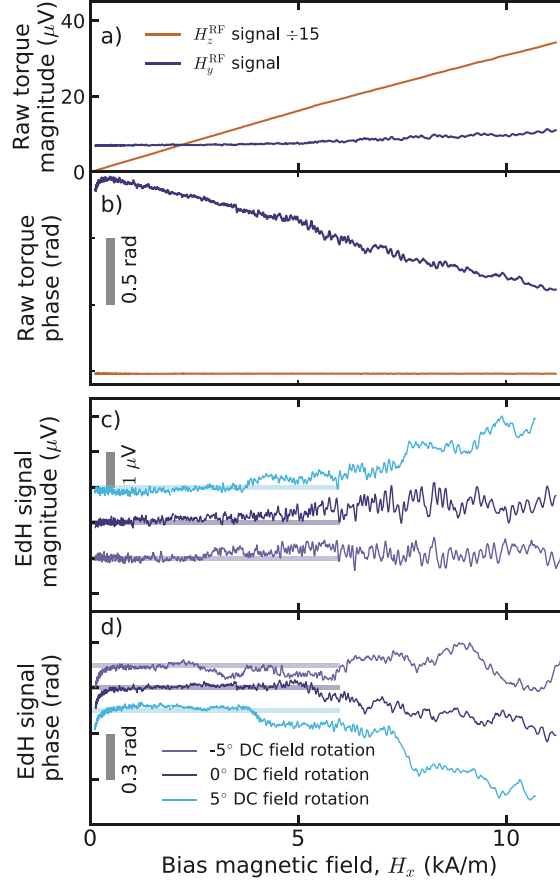


Figure 2.13: Extension of simultaneous (phase-locked) measurement of H_y^{RF} driven EdH and H_z^{RF} driven cross-product torques throughout the field range that encompasses the vortex state. The field is swept low (L) to high (H) and then H to L. Panels a) and b) represent the unmodified 'raw' magnitude and phase respectively. The linear increase in EdH magnitude and decrease in phase are indicative of cross-product admixture. Panels c) and d) represent the EdH signal where the admixture of cross-product torque has been removed. The remaining features indicate that the EdH torque and phase are sensitive probes of magnetic disorder and surface roughness. The low field phase drift that appears in panel d) is indicative of the PLL losing the reference phase as the signal-to-noise ratio of the cross-product torques becomes too large.

lags behind the cross product torque. Admixture of driving field contributions also explains the gradual increase in EdH signal magnitude. The admixture can be easily removed from the H_y^{RF} driven signal due to the quadrature phase sensitivity of the lock-in measurements. Based on subtraction of quadrature component, we found that the admixture of torques amounted to 1.2% of the slope of the raw H_y^{RF} driven phase

signal. An admixture constant was found by multiplying the slope of the decreasing signal with the raw H_z^{RF} driven signal, we subtracted this from the quadrature component of the EdH. Panels c) and d) show the H_y^{RF} driven signal following the removal of the admixture from the EdH torque magnitude and phase. We also introduced a rotation of the DC magnetic field by $\pm 5^\circ$ from the positive x axis. For ease of visibility, a $1 \mu\text{V}$ offset was applied to each signal in panel c), and an offset of 0.15 rad was applied to each trace in panel d).

As seen in panel c) and d) of Figure 2.13, even after subtracting the admixture of the cross-product torque signal, the EdH signal magnitude exhibited different behaviour that is highly sensitive to the angle of the DC magnet. This angular dependence of applied field is due to the particular sensitivity of EdH signal to magnetic disorder and sample surface roughness. Cross-product measurements indicate that vortex core pinning is not a pronounced effect for this sample due to the YIG disks monocrystallinity and exceptional purity. Unlike the cross-product torque, however, EdH torques should be much more sensitive to sample surface roughness in the vortex state. Micromagnetic simulations of the vortex state in 0.23 aspect ratio ferromagnetic cylinders indicate that the vortex core dilates in the centre of the sample (corroborated by results of [42]), ergo the core has a narrower diameter at the surfaces than found in the bulk of the YIG disk. To consider the effect of the fields for a cross-product torque measurement on the vortex structure, an in-plane DC bias is introduced, and an out-of-plane AC field is applied. Since the in plane field is static, the generation of the torque does not occur by way of vortex core translation, only a dilation and contraction. This core dilation and contraction is a roughly negligible effect on the spin texture, however it may permit the core to hop between closely spaced energy minima and cross-product torques will yield the time averaged position of the core. The effect of vortex pinning in a ferromagnetic thin film is described at length by Burgess et al. [32].

The field applied to generate an EdH torque (unlike the cross-product torque)

varies the core position since the alternating field is applied in-plane, one may think of this as an alternating translation of the vortex core perpendicular to the AC field direction. The core, in this way, can act as a very sensitive probe to magnetic disorder and shape imperfections that are of similar size to the core.

Simultaneous Measurement of Cross-product and EdH Torques Beyond Vortex Annihilation

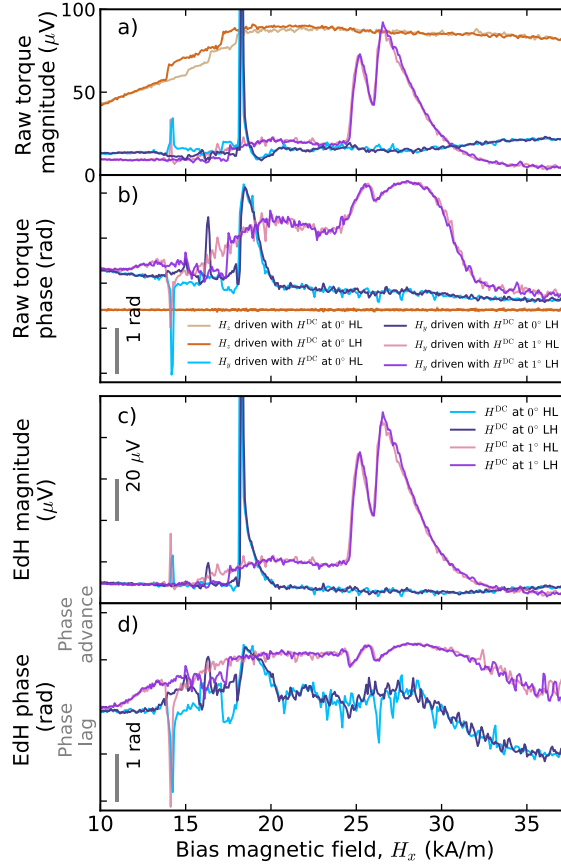


Figure 2.14: High field hysteresis loops extend to field strengths greater than those that permit vortex spin textures. The irreversible vortex annihilation occurs around 18 kA/m. This spin texture change is observed both in the EdH (as spikes in magnitude and phase) and cross-product torque signals (as discontinuous jumps in magnitude). The spikes that are cut off in panels a) and c) extend to 150 μV . Two magnet rotation positions are shown, 0° , and 1° indicating a striking dependence of bias magnetic field angle on EdH torques.

The continued extension to the high-field regime results in the annihilation of the vortex state, giving way to the quasi-uniform spin texture. This spin texture consists

of a mostly uniformly oriented magnetization, with the emergence of closure domains close to the edge of the magnet. The vortex nucleation can be clearly seen in panel a) of Figure 2.14 where the cross-product torque signal irreversibly increased in magnitude close to 14 kA/m. The magnet was fully saturated at 20 kA/m, and beyond this field the cross-product torque magnitude began to monotonically decrease. We have already encountered a hysteresis loop of this kind in Section 2.3.1. In Figure 2.14 panel b), the cross-product torque phase is plotted and there was clearly no phase deviation over the experimental field range. The EdH torque signal magnitude and phase, panel b) and d), however are drastically altered in this quasi-static regime, exhibiting large changes in magnitude and phase where no such behaviour was observed in the cross-product torque. The most striking of these features is the large reversible peaks that emerge for the 1° rotated DC bias field between 24 kA/m and 33 kA/m. These peaks are completely absent from the 0° rotated field, indicating a strong dependence on bias field direction.

Previously, behaviour in the EdH signal magnitude and phase was attributed to the RF translational motion of the vortex core. In the field region from 18 kA/m onward of Figure 2.14, the vortex spin texture annihilates and enters the quasi-uniform state. As we did for the vortex state, we once again consider the effect of in-plane fields on the magnetic spin texture. An alternating field in the plane of the quasi-uniformly magnetized YIG cylinder modulates the position of closure domain walls. This, again is not an effect that the cross-product torque is sensitive to since the only applied in-plane field is static and does not rapidly modulate the position of the domain walls. Vortex state measurements of cross-product torques indicated that the sample interior is extremely pure since no discernible vortex core pinning is observed, however EdH signals yield information about surface roughness. In the high field regime closure domains can interact with the edges of the sample, which, due to fabrication are rough. In this case, a field that modulates the position of the closure domain walls about the edge of the sample would, in fact, serve as a probe, sensitive to edge roughness of the

cylinder wall.

The phase exhibited by the EdH signal in panel d) of Figure 2.14 elucidates the relationship between the magnetic behaviour as it relates to the transfer of angular momentum to the lattice. We hypothesize if the applied RF field, H_y^{RF} , is alternating faster than the angular momentum transfer can occur, a phase delay is expected at rates faster than the rate of angular momentum transfer. A more in-depth description of future work studying EdH physics at ever higher frequencies is provided in Section 3.2. An effect of phase lag certainly appears to have begun around 30 kA/m in both bias field angle positions. The full picture of high field EdH torque phase, however is more complicated than this. A very pronounced phase advance is observed in the 1° rotation trace. An ideal method for studying the effect of edge roughness on EdH experiments can be made through micromagnetic simulations that, in effect, have built-in edge roughness for simulations of cylindrical ferromagnets. This will be our next point of discussion

2.3.5 Micromagnetic Simulations of Einstein-de Haas Experiments

Earlier discussions of micromagnetic simulations served to give an accurate measurement of magnetic aspect ratio. By revisiting micromagnetic simulations we will calculate high field hysteresis behaviour in EdH torque signals where edge roughness is present. Unlike previous discussions however, here we will discuss, in addition to cross-product torques, micromagnetically simulated EdH torques. Mumax3 returns volume averaged magnetization, field and energy terms. The EdH torque (as described in Section 2.1) is given by

$$\vec{\tau}^{\text{EdH}} = -\frac{d\vec{J}}{dt} = -\frac{2m_e}{eg'} \frac{d\vec{m}}{dt} \quad (2.28)$$

As described in Section 2.3.4, the present work was conducted at sufficiently low frequency that we do not expect dynamics to play a role in experimental results and the usual method for calculating the torque can be performed. In this case, as before,

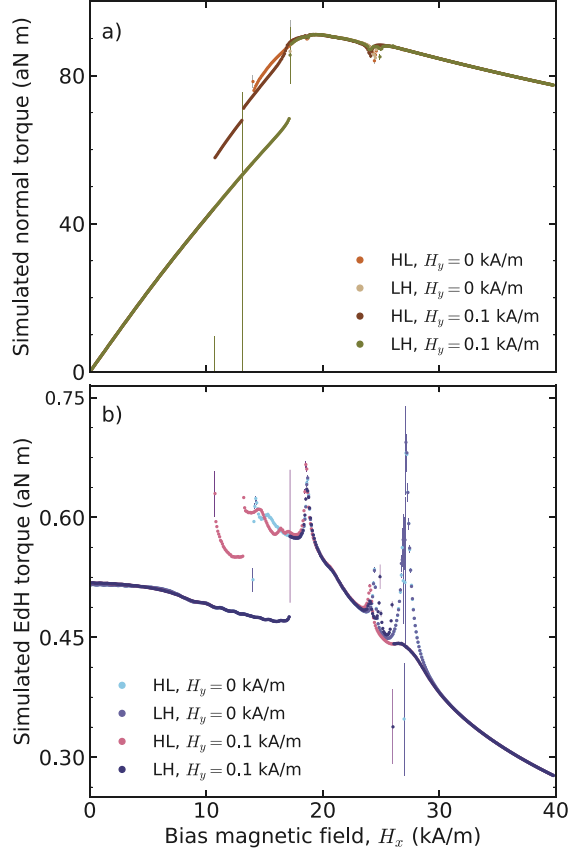


Figure 2.15: Simulation outputs for a high field hysteresis measurement wherein cross-product torques are shown in panel a) and EdH torque simulation results are shown in panel b). Bias field offsets of 0.1 kA/m in the y direction are also applied to simulate an applied field at an offset angle. As in the experimental case, this offset has little impact on cross-product torques, however panel b) represents some drastic changes in behaviour between the bias field direction, such as, the large peak around 26 kA/m which is not only unique to the $H_y = 0$ kA/m trace, but is not present in the cross-product torque signal.

the time is not exactly calculated since at each field step, the system relaxes to an equilibrium configuration. In the language of the LLG equation, this is the timescale when the damping term dominates the precession term. Our time-varying field, is then replaced by a magnetic field along the dither directions (in this case, z and y , as in the experiment). The dither field is varied between DC field steps in a hysteresis loop from the quasiuniform state at 40 kA/m to the vortex spin texture at 0 kA/m and back.

Micromagnetic simulations make excellent candidates for capturing effects of edge

roughness on magnetic torque signals since mumax3 builds its geometry on a grid of rectangular prisms. This means that a cylinder has a built-in edge roughness that is brought about simply by the approximation of a circle on a grid. We expect in this case that the roughness will have some effect on the EdH torque signal that is calculated from simulation results due to the driving field modulating closure domain wall positions.

The results of a high field hysteresis measurement can be found in Figure 2.15. To represent a change in bias field direction, we introduced a 0.1 kA/m offset along the y axis. This offset acts as an effective rotation of the bias field direction which can be compared with the case of no rotation. Panel a) represents the normal simulated cross-product torque, and as can be seen, there is a difference between the positions of nucleation, where a transitional spin texture appears between 11 kA/m and 13 kA/m, otherwise the trends are quite similar. Panel b) shows the simulated EdH torque. Here the EdH torque was calculated using the experimentally determined ratio of $\frac{f}{g'} = \frac{2.7904 \text{ MHz}}{1.8}$. A striking feature is observed at the 26 kA/m bias field step where a prominent peak appears in the $H_y = 0$ kA/m simulated hysteresis. This peak is much smaller in the $H_y = 0.1$ kA/m hysteresis loop.

Here we have presented the usefulness of micromagnetic simulations to predict results of EdH experiments. Built-in edge roughness makes the grid-layout of mumax3 simulations ideal for predicting EdH torques in ferromagnets. While the EdH torques are modulated at frequencies that are low enough to not encounter dynamical effects, mumax3 is well suited to time dependent studies of such a situation. In the next chapter, we will formulate the hypothesis that linear scaling of EdH torque magnitudes with frequency must break down at a sufficiently high frequency, dictated by the spin-lattice relaxation rate. Micromagnetic simulations, such as those presented here, serve as an important jumping-off-point for predicting results of future work at high frequency.

Chapter 3

Conclusions & Future Work

3.1 Conclusions

In conclusion, this revisiting of the Einstein-de Haas (EdH) experiment has expanded on modern trends of EdH experiment miniaturization, and increased the frequency of applied EdH torque from the audio frequency range to the radio frequency range. Linear scaling of EdH torque with frequency permits magnitudes of EdH torques, that are of the same scale, or larger than cross-product torques. By simultaneously demodulating EdH and cross-product torques, another important quality of EdH torques was observed: the relative phase difference between driving field and EdH torque signal that is a consequence of the time rate of change of angular momentum. Such a definition indicates that EdH torques has a 90° phase difference when compared to conventional cross-product torques. Our results confirmed that EdH torques are larger than cross-product torques in some DC field regions for RF drive levels, and verified the 90° phase shift, which confirmed the distinct origin of each torque signal. The simultaneous measurement of EdH and cross-product torques was also used to obtain the magnetomechanical factor, which was found to be $g' = 1.78 \pm 0.16$, for YIG. This is the first measurement of g' in a YIG sample. Previous estimates for g' suggest that, if the relation $2 - g' \approx g - 2$ holds, our result is within 2 standard deviations from the expected value for g' based on results for g from Dillon [41].

Enabled by highly uniform driving field geometries, EdH torque measurements

were brought to high field where the vortex core behaves like a sensitive probe of magnetic surface defects in mesoscopic YIG disks. This sensitivity is evidenced by EdH torque magnitude fluctuations that are altogether absent in cross-product torque signals. One reason this occurs is due to the dither field required for creating an EdH torque. The application of this field modulates the vortex cores position, unlike in the case of the cross-product case where the vortex core diameter is modulated.

By extending the field beyond vortex annihilation, we observed EdH torques in the quasi-uniform spin texture state. In this state, the EdH torque is sensitive to edge roughness about the circumference of the YIG disk via modulation of closure domain wall position. We can thus use the EdH torque as a sensitive probe of the YIG cylinder surface, and control which surface we are probing by applying a larger magnetic field. Mumax3 simulations of EdH and cross-product torques indicate a significant dependence on field angle brought forth by edge roughness observed in the experiment.

3.2 Future Work

The experiment detailed in this thesis is simply a jumping-off-point for an extensive list of future projects. There is still a great deal to be understood about angular momentum conservation in magnetic systems and EdH experiments are an invaluable tool for the understanding of angular momentum conservation processes. The unique way that EdH torques manifest compared to cross-product torques situates the effect as an ideal tool for study of interfacial effects for magnetic sample characterization.

3.2.1 Spin-Lattice Relaxation from the Perspective of the Lattice

We propose that extensions of EdH experiments to higher and higher frequencies will eventually reach a limit wherein the linear relation between EdH torques and frequency breaks down. This limit, we expect is mediated by the spin-lattice relaxation

time. We might expect such a behaviour to be most obviously observed by a phase lag in the EdH torque as the driving field begins to out-pace the transfer of angular momentum. This would provide a direct measurement of T_1 for ordered magnetic systems. This method need not be confined to ferro-, or ferri- magnets, but antiferromagnets may also be measured this way. Theoretical studies of phonon spin effects, and their role in EdH experiments have separated rigid body motion from internal angular momentum [43]. The onset of this separation is what we hope to observe in experiments of UHF EdH experiments.

Beyond ordered magnets, there is the extremely promising avenue of EdH experiments on nuclear paramagnets. Recently, the Barnett effect of magnetization by rotation was observed by M. Arabgol and T. Sleator [44] while the inverse effect of rotation by magnetization has yet to be observed. In keeping with the theme of measuring spin lattice relaxation from the perspective of the lattice; judicious selection of plastic crystals that permit rotation of molecules could be used to compare T_1 with the spin-lattice relaxation in the rotating frame, $T_{1,\text{rot}}$. Adamantane is an early contender for such a study.

3.2.2 Time Rate of Change of Angular Momentum in Superconductors

Beyond conventional magnetic ordering, EdH experiments may also be used to study superconductors. So far, EdH experiments have only been performed on conventional Type-I superconductors [45]. No magnetomechanical experiments have been performed on type-II, or unconventional superconductors. Aside from several (quite old) examples, torque experiments on superconducting materials have exclusively featured cross-product torques. There is also theoretical interest in the time rate of change of angular momentum experiments in superconductors [46, 47].

Once again cross-product and EdH torques can be simultaneously studied in superconductors opening the door to studies of superconductor RF susceptibilities,

fixed magnetization contributions to cross-product torque, field dependencies, and frequency dependencies. We predict that superconductor EdH torques should not be dramatically smaller than those presented in this thesis based on the relatively low magnetic susceptibility of YIG compared to the diamagnetic susceptibility of a superconductor. All else being equal, the measured values of susceptibility of YIG in the vortex state [48] yield EdH torques 4-5 times larger than that of a perfectly diamagnetic superconductor. This susceptibility places measurements of EdH torques on superconductors well within reach.

3.2.3 Six-‘axis’ AC Torque Magnetometry

Recent developments in AC torque magnetometry have shown that vector torque magnetometry is an extremely exciting avenue of research [49–51]. I propose that each mechanical axis of torque need not only measure one kind of torque, but a cross-product, and EdH torque. This, in effect, gives the experimenter a greater variety of tools for investigation of magnetic materials. A recent study of permalloy / cobalt oxide bilayers that display the exchange bias effect below the CoO Neel temperature used three axis AC torque magnetometry to study anisotropies within the magnetic sample [52]. I have emphasized the influence of interfacial effects on EdH torques here; I suspect for monocrystalline exchange bias samples, EdH could lend insight into interfacial features of bilayer FM/AFM systems.

Bibliography

- [1] S. Chikazumi and C. D. Graham, *Physics of Ferromagnetism 2e*, 94. Oxford University Press on Demand, 2009.
- [2] S. Malin and D. Barraclough, “150th anniversary of Gauss’s first absolute magnetic measurement,” *Nature*, vol. 297, no. 5864, pp. 285–285, 1982.
- [3] A. Einstein and W. J. de Haas, “Magnetometer proof of the existence of Ampere’s molecular currents,” *Proceedings - KNAW*, vol. 18, p. 696, 1915.
- [4] N. Bohr, *Studier over metallernes elektrontheori*. Thaning & Appel in Komm., 1911.
- [5] H. Van Leeuwen, “Problemes de la théorie électronique du magnétisme,” *J. Phys. Radium*, vol. 2, no. 12, pp. 361–377, 1921.
- [6] J. Van Vleck, *The Theory of Electric and Magnetic Susceptibilities*, ser. International series of monographs on physics. Oxford University Press, 1965. [Online]. Available: <https://books.google.ca/books?id=5GQGAQAIAAJ>.
- [7] G. H. O. Daalderop, P. J. Kelly, and M. F. H. Schuurmans, “First-principles calculation of the magnetocrystalline anisotropy energy of iron, cobalt, and nickel,” *Phys. Rev. B*, vol. 41, pp. 11 919–11 937, 17 1990. DOI: 10.1103/PhysRevB.41.11919. [Online]. Available: <https://link.aps.org/doi/10.1103/PhysRevB.41.11919>.
- [8] S Geller and M. Gilleo, “Structure and ferrimagnetism of yttrium and rare-earth–iron garnets,” *Acta Crystallographica*, vol. 10, no. 3, pp. 239–239, 1957.
- [9] O. W. Richardson, “A mechanical effect accompanying magnetization,” *Physical Review (Series I)*, vol. 26, no. 3, p. 248, 1908.
- [10] P. Galison and J. Galison, *How Experiments End*, ser. A Chicago original paperback. University of Chicago Press, 1987, ISBN: 9780226279152. [Online]. Available: <https://books.google.ca/books?id=ysWp7LTHor4C>.
- [11] W. Sucksmith and L. F. Bates, “On a null method of measuring the gyromagnetic ratio,” *Proceedings of the Royal Society of London. Series A, Containing Papers of a Mathematical and Physical Character*, vol. 104, no. 727, pp. 499–511, 1923.
- [12] S. J. Barnett, “Gyromagnetic and electron-inertia effects,” *Rev. Mod. Phys.*, vol. 7, pp. 129–166, 2 1935. DOI: 10.1103/RevModPhys.7.129. [Online]. Available: <https://link.aps.org/doi/10.1103/RevModPhys.7.129>.

- [13] G. G. Scott, “Review of gyromagnetic ratio experiments,” *Rev. Mod. Phys.*, vol. 34, pp. 102–109, 1 1962. DOI: 10.1103/RevModPhys.34.102. [Online]. Available: <https://link.aps.org/doi/10.1103/RevModPhys.34.102>.
- [14] C. Kittel, “On the gyromagnetic ratio and spectroscopic splitting factor of ferromagnetic substances,” *Phys. Rev.*, vol. 76, pp. 743–748, 6 1949. DOI: 10.1103/PhysRev.76.743. [Online]. Available: <https://link.aps.org/doi/10.1103/PhysRev.76.743>.
- [15] B. Cullity and C. Graham, *Introduction to Magnetic Materials*. Wiley, 2009, ISBN: 9780470386316. [Online]. Available: <https://books.google.ca/books?id=kk1el8vB4HoC>.
- [16] S. Blundell, *Magnetism in Condensed Matter*, ser. Oxford Master Series in Condensed Matter Physics. OUP Oxford, 2001, ISBN: 9780198505914. [Online]. Available: <https://books.google.ca/books?id=OGhGmgEACAAJ>.
- [17] H. Williams, “Some uses of the torque magnetometer,” *Review of Scientific Instruments*, vol. 8, no. 2, pp. 56–60, 1937.
- [18] R. Kleiman, G. Kaminsky, J. Reppy, R Pindak, and D. Bishop, “Single-crystal silicon high-Q torsional oscillators,” *Review of scientific instruments*, vol. 56, no. 11, pp. 2088–2091, 1985.
- [19] P. Crowell, A Madouri, M Specht, G Chaboussant, D Mailly, and L. Levy, “Torsional oscillator magnetometer for high magnetic fields,” *Review of scientific instruments*, vol. 67, no. 12, pp. 4161–4166, 1996.
- [20] R. Biggar and J. Parpia, “High-Q oscillator torque magnetometer,” *Review of scientific instruments*, vol. 69, no. 10, pp. 3558–3562, 1998.
- [21] M. D. Chabot and J. Moreland, “Micrometer-scale magnetometry of thin Ni₈₀Fe₂₀ films using ultrasensitive microcantilevers,” *Journal of applied physics*, vol. 93, no. 10, pp. 7897–7899, 2003.
- [22] J. Davis, D. Vick, D. Fortin, J. Burgess, W. Hiebert, and M. Freeman, “Nanotorsional resonator torque magnetometry,” *Applied Physics Letters*, vol. 96, no. 7, p. 072513, 2010.
- [23] T. M. Wallis, J. Moreland, and P. Kabos, “Einstein-de Haas effect in a NiFe film deposited on a microcantilever,” *Appl. Phys. Lett.*, vol. 89, pp. 122502–1–122502–3, 2006.
- [24] W. Brown, *Micromagnetics*, ser. Interscience tracts on physics and astronomy. J. Wiley, 1963. [Online]. Available: <https://books.google.ca/books?id=0XMSMQAACA AJ>.
- [25] T. Gilbert and J. Kelly, “Anomalous rotational damping in ferromagnetic sheets,” *Conference on Magnetism and Magnetic Materials, Pittsburgh, PA, June 14–16, 1955*.
- [26] T. L. Gilbert, “A phenomenological theory of damping in ferromagnetic materials,” *IEEE transactions on magnetics*, vol. 40, no. 6, pp. 3443–3449, 2004.

- [27] W. H. Meiklejohn and C. P. Bean, “New magnetic anisotropy,” *Phys. Rev.*, vol. 105, pp. 904–913, 3 1957. DOI: 10.1103/PhysRev.105.904. [Online]. Available: <https://link.aps.org/doi/10.1103/PhysRev.105.904>.
- [28] R. I. Joseph, “Ballistic demagnetizing factor in uniformly magnetized cylinders,” *Journal of applied physics*, vol. 37, no. 13, pp. 4639–4643, 1966.
- [29] M. Beleggia, M. De Graef, and Y. T. Millev, “Demagnetization factors of the general ellipsoid: An alternative to the Maxwell approach,” *Phil. Mag.*, vol. 86, pp. 2451–2466, 2006.
- [30] M. J. Donahue and M. Donahue, *OOMMF user’s guide, version 1.0*. US Department of Commerce, National Institute of Standards and Technology, 1999.
- [31] A. Vansteenkiste, J. Leliaert, M. Dvornik, M. Helsen, F. Garcia-Sanchez, and B. Van Waeyenberge, “The design and verification of mumax3,” *AIP advances*, vol. 4, no. 10, p. 107133, 2014.
- [32] J. A. J. Burgess, A. E. Fraser, F. Fani Sani, D. Vick, B. D. Hauer, J. P. Davis, and M. R. Freeman, “Quantitative magneto-mechanical detection and control of the Barkhausen effect,” *Science*, vol. 339, p. 1051, 2013.
- [33] K. Mori, M. G. Dunsmore, J. E. Losby, D. M. Jenson, M. Belov, and M. R. Freeman, “Einstein–de Haas effect at radio frequencies in and near magnetic equilibrium,” *Phys. Rev. B*, vol. 102, p. 054415, 5 2020. DOI: 10.1103/PhysRevB.102.054415. [Online]. Available: <https://link.aps.org/doi/10.1103/PhysRevB.102.054415>.
- [34] J. Q. Stewart., “The moment of momentum accompanying magnetic moment in iron and nickel,” *Phys. Rev.*, vol. 11, pp. 100–120, 2 1918. DOI: 10.1103/PhysRev.11.100. [Online]. Available: <https://link.aps.org/doi/10.1103/PhysRev.11.100>.
- [35] *COMSOL Multiphysics (TM)*. [Online]. Available: <https://www.comsol.com/>.
- [36] A. Fraser, “Focused ion beam milled magnetic cantilevers,” 2010.
- [37] M. R. Freeman, “Method for measuring current distribution in an integrated circuit by detecting magneto-optic polarization rotation in an adjacent magneto-optic film,” US Patent Number 5,663,652, Tech. Rep., 1997.
- [38] J. Losby, J. A. J. Burgess, Z. Diao, D. C. Fortin, W. K. Hiebert, and M. R. Freeman, “Thermo-mechanical sensitivity calibration of nanotorsional magnetometers,” *Journal of Applied Physics*, vol. 111, no. 7, p. 07D305, 2012. DOI: 10.1063/1.3676231. eprint: <https://doi.org/10.1063/1.3676231>. [Online]. Available: <https://doi.org/10.1063/1.3676231>.
- [39] A. N. Cleland and M. L. Roukes, “Noise processes in nanomechanical resonators,” *Journal of applied physics*, vol. 92, no. 5, pp. 2758–2769, 2002.
- [40] B. Hauer, C Doolin, K. Beach, and J. Davis, “A general procedure for thermo-mechanical calibration of nano/micro-mechanical resonators,” *Annals of Physics*, vol. 339, pp. 181–207, 2013.

- [41] J. F. Dillon, “Ferrimagnetic resonance in yttrium iron garnet,” *Phys. Rev.*, vol. 105, pp. 759–760, 2 1957. DOI: 10.1103/PhysRev.105.759. [Online]. Available: <https://link.aps.org/doi/10.1103/PhysRev.105.759>.
- [42] O. V. Pylypovskiy, D. D. Sheka, V. P. Kravchuk, and Y. Gaididei, “Effects of surface anisotropy on magnetic vortex core,” *Journal of magnetism and magnetic materials*, vol. 361, pp. 201–205, 2014.
- [43] A. Rückriegel, S. Streib, G. E. W. Bauer, and R. A. Duine, “Angular momentum conservation and phonon spin in magnetic insulators,” *Phys. Rev. B*, vol. 101, p. 104 402, 10 2020. DOI: 10.1103/PhysRevB.101.104402. [Online]. Available: <https://link.aps.org/doi/10.1103/PhysRevB.101.104402>.
- [44] M. Arabgol and T. Sleator, “Observation of the nuclear barnett effect,” *Phys. Rev. Lett.*, vol. 122, p. 177 202, 17 2019. DOI: 10.1103/PhysRevLett.122.177202. [Online]. Available: <https://link.aps.org/doi/10.1103/PhysRevLett.122.177202>.
- [45] R. H. Pry, A. L. Lathrop, and W. V. Houston, “Gyromagnetic effect in a superconductor,” *Phys. Rev.*, vol. 86, pp. 905–907, 6 1952. DOI: 10.1103/PhysRev.86.905. [Online]. Available: <https://link.aps.org/doi/10.1103/PhysRev.86.905>.
- [46] J. Hirsch, “The missing angular momentum of superconductors,” *Journal of Physics: Condensed Matter*, vol. 20, no. 23, p. 235 233, 2008.
- [47] J. Hirsch, “On the reversibility of the meissner effect and the angular momentum puzzle,” *Annals of Physics*, vol. 373, pp. 230–244, 2016.
- [48] J. Losby, F. F. Sani, D. Grandmont, Z. Diao, M. Belov, J. Burgess, S. Compton, W. Hiebert, D. Vick, K. Mohammad, *et al.*, “Torque-mixing magnetic resonance spectroscopy,” *Science*, vol. 350, no. 6262, pp. 798–801, 2015.
- [49] G. Hajisalem, J. E. Losby, G. de Oliveira Luiz, V. T. Sauer, P. E. Barclay, and M. R. Freeman, “Two-axis cavity optomechanical torque characterization of magnetic microstructures,” *New Journal of Physics*, vol. 21, no. 9, p. 095 005, 2019.
- [50] H Mattiat, N Rossi, B Gross, J. Pablo-Navarro, C. Magén, R Badea, J Berzovsky, J. De Teresa, and M Poggio, “Nanowire magnetic force sensors fabricated by focused-electron-beam-induced deposition,” *Physical Review Applied*, vol. 13, no. 4, p. 044 043, 2020.
- [51] K. Fast, J. Thibault, V. Sauer, M. Dunsmore, A Kav, J. Losby, Z Diao, E. Luber, M Belov, and M. Freeman, “Simultaneous three-axis torque measurements of micromagnetism,” *AIP Advances*, vol. 11, no. 1, p. 015 119, 2021.
- [52] M. Dunsmore, J. Thibault, K. Fast, V. Sauer, J. Losby, Z Diao, M Belov, and M. Freeman, “Three-axis torque investigation of interfacial exchange coupling in a NiFe/CoO bilayer micromagnetic disk,” *AIP Advances*, vol. 12, no. 3, p. 035 142, 2022.

Appendix A: Equivalence of Cross Product and Energy Differential Torque

Here we will draw the connection between the cross product torque, generated by the relative orientations of magnetization \vec{m} and effective field \vec{H}

$$\vec{\tau} = \mu_0 \vec{m} \times \vec{H}, \quad (\text{A.1})$$

and the differential representation of this same formula for torque along an axis i

$$\tau_i = -V \frac{d\varepsilon}{d\theta}. \quad (\text{A.2})$$

We begin by rewriting the differential form of the torque as a dot product relation, choosing one axis i with unit vector \hat{n}

$$\hat{n} \cdot \vec{\tau} = -V \frac{d\varepsilon}{d\theta}. \quad (\text{A.3})$$

The chain rule is evoked to write

$$\hat{n} \cdot \vec{\tau} = -V \frac{d\varepsilon}{d\vec{m}} \frac{d\vec{m}}{d\theta}. \quad (\text{A.4})$$

The effective field can be given by the functional derivative of energy with respect to magnetization $\vec{H}_{\text{eff}} = V \frac{\partial \varepsilon}{\partial \vec{m}}$, we find

$$\hat{n} \cdot \vec{\tau} = \mu_0 \frac{d\vec{m}}{d\theta} \cdot \vec{H}_{\text{eff}} \quad (\text{A.5})$$

We now consider the general form of the rotation of the magnetization vector \vec{m} to some new rotated vector \vec{m}' by an angle θ

$$\vec{m}' = \vec{m} \cos(\theta) + \hat{n}(\hat{n} \cdot \vec{m})(1 - \cos(\theta)) + (\hat{n} \times \vec{m}). \quad (\text{A.6})$$

For an infinitesimal rotation $d\theta$: $\cos(d\theta) \sim 1$ and $\sin(d\theta) \sim d\theta$. This gives us

$$\vec{m}' = \vec{m} + (\hat{n} \times \vec{m})d\theta \quad (\text{A.7})$$

We can rearrange the above equation, recognizing that an infinitesimal rotation yields $\vec{m}' - \vec{m} = d\vec{m}$ so $\frac{d\vec{m}}{d\theta} = \hat{n} \times \vec{m}$. Plugging this relation into equation A.5, we find

$$\hat{n} \cdot \vec{\tau} = \mu_0(\hat{n} \times \vec{m}) \cdot \vec{H}_{\text{eff}} \quad (\text{A.8})$$

Finally we generalize the right and left hand side, using the scalar triple product

$$\vec{\tau} = \mu_0 \vec{m} \times \vec{H}_{\text{eff}} \quad (\text{A.9})$$

Appendix B: Sample Code for Macrospin Simulation

As shown in Section 1.4, the LLG equation can be rearranged in the following way

$$\begin{aligned}\frac{d\theta}{dt} &= \frac{-\gamma}{M_s(1+\alpha^2)} \left(\frac{1}{\sin(\theta)} \frac{\partial \varepsilon}{\partial \phi} + \alpha \frac{\partial \varepsilon}{\partial \theta} \right) \\ \frac{d\phi}{dt} &= \frac{\gamma}{M_s(1+\alpha^2)} \left(\frac{\alpha}{\sin^2(\theta)} \frac{\partial \varepsilon}{\partial \phi} - \frac{1}{\sin(\theta)} \frac{\partial \varepsilon}{\partial \theta} \right).\end{aligned}\tag{B.1}$$

This form is particularly useful since we have converted from cartesian coordinates (with three unknowns) to spherical coordinates (with two unknowns since $\frac{dM_r}{dt} = 0$ by definition). Below I have presented the code used to generate the simulation result found in Figure 1.6.

Listing B.1: LLG equation for a single spin. The shape is dictated by demagnetizing factors $N_{x,y,z}$. The equation used to solve the equation of motion is presented in Equation B.1.

```
#!/usr/bin/env python3
# -*- coding: utf-8 -*-
"""
Created on Fri Dec 3 11:49:32 2021

@author: michaeldunsmore
"""

import numpy as np
from scipy.integrate import solve_ivp
import matplotlib.pyplot as plt

# physical constants
u0 = 4*np.pi*1e-7 #N/A^2
#gamma = 0.176 #ps^-1 T^-1
#Note! If using value output via mumax 3, units are in rad/(ns*T)
gamma = 175.95/(np.pi*2) #ns^-1 T^-1
alpha = 0.01
Kua = 1e3 #J/m^3
M = 763000 #A/m
fieldang=0*np.pi/4
# bias field
dither=100
Hx2=(10000)*np.cos(fieldang)+dither #A/m
Hy2=(10000)*np.sin(fieldang)+dither #A/m
Hz2=dither*np.cos(np.pi/2) #A/m
```

```

H = np.array([Hx2,Hy2,Hz2]) #A/m
print(np.arctan2(Hy2,Hx2))
# demag factors (for a sphere)
Nx = 1/3
Ny = 1/3
Nz = 1/3

#Energy density terms

def WA(the, phi):
    return -Kua*(np.sin(the)*np.cos(phi))**2

def WD(the, phi):
    return 0.5*u0*(M**2)*(Nz*(np.cos(the)**2) + Ny*(np.cos(phi)**2)
        + Nx*(np.sin(phi)**2))

def WZ(the, phi, Hx1, Hy1, Hz1):
    return -u0*M*(Hx1*np.sin(the)*np.cos(phi)+Hy1*np.sin(the)*np.sin(phi)
        +Hz1*np.cos(the))

def Wtot(the, phi, Hx1, Hy1, Hz1):
    return WA(the, phi)+WD(the, phi)+WZ(the, phi, Hx1, Hy1, Hz1)

#Partial derivative of anisotropy terms with respect to azimuthal angle

def dtheWA(the, phi):
    return -2*Kua*np.sin(the)*np.cos(the)*(np.cos(phi)**2)*gamma/(M)

def dtheWD(the, phi):
    return -(gamma*M*u0)*Nz*np.sin(the)*np.cos(the)

def dtheWZ(the, phi, Hx1, Hy1, Hz1):
    return -(gamma*u0)*(Hx1*np.cos(the)*np.cos(phi)+Hy1*np.cos(the)*np.sin(phi)
        -Hz1*np.sin(the))

def dtheW(the, phi, Hx1, Hy1, Hz1):
    return dtheWA(the, phi)+dtheWD(the, phi)+dtheWZ(the, phi, Hx1, Hy1, Hz1)

#Partial derivative of anisotropy terms with respect to polar angle

def dphiWA(the, phi):
    return 2*gamma*Kua*(np.sin(the)**2)*np.sin(phi)*np.cos(phi)/(M)

def dphiWD(the, phi):
    return (gamma*M*u0)*(-Nx*np.sin(phi)*np.cos(phi) + Ny*np.cos(phi)*np.sin(phi))

def dphiWZ(the, phi, Hx1, Hy1):
    return -(gamma*u0)*(-Hx1*np.sin(the)*np.sin(phi)+Hy1*np.sin(the)*np.cos(phi))

def dphiW(the, phi, Hx1, Hy1):
    return dphiWA(the, phi) + dphiWZ(the, phi, Hx1, Hy1) + dphiWD(the, phi)

N=10000

t_vals=np.linspace(0,200,N)
def ode(t,y):

    #Hz=0*np.cos(omega*t)
    Hz=Hz2#+50*np.sin(omega*t/0.01)
    Hy=Hy2#+(1000/4.7462)*np.sin(omega*t)
    Hx=Hx2#+(50/4.7462)*np.sin(omega*t)
    the=y[0]
    phi=y[1]
    thetadot=(1/(np.sin(the)*(1+alpha**2)))*((-1)*dphiW(the, phi, Hx, Hy)
        -alpha*np.sin(the)*dtheW(the, phi, Hx, Hy, Hz))
    phidot=(1/((np.sin(the)**2)*(1+alpha**2)))*((-alpha)*dphiW(the, phi, Hx, Hy)

```

```

+np.sin(the)*dtheW(the,phi,Hx,Hy,Hz)
out = [thetadot, phidot]
return out

#t_vals=np.arange(0,0.01,0.01)

sol = solve_ivp(ode,[0,200],[np.pi/2,np.pi/2],t_eval=t_vals,method='Radau')

mx = np.multiply(np.sin(sol.y[0]),np.cos(sol.y[1]))
my = np.multiply(np.sin(sol.y[0]),np.sin(sol.y[1]))
mz = np.cos(sol.y[0])

m = np.sqrt(np.multiply(mx,mx)+np.multiply(my,my)+np.multiply(mz,mz))

plt.figure(1,figsize=(8,5))
plt.plot(sol.t,mx,'-',color='deepskyblue',label='$M_{x}/M_{s}$')
plt.plot(sol.t,my,'-',color='slateblue',label='$M_{y}/M_{s}$')
plt.plot(sol.t,mz,'-',color='chocolate',label='$M_{z}/M_{s}$')
plt.plot(sol.t,m,'-',color='black',label='$M/M_{s}$')
plt.xlabel('Time (ns)',fontsize=14)
plt.legend(fontsize=12,frameon=False)
plt.ylabel('Magnetization component\nnormalized by $M_{S}$',fontsize=14)

tau=np.zeros((np.size(mx),3))
print()
for i in range(np.size(mx)):
    tau[i]=np.cross([mx[i],my[i],mz[i]],[Hx2,Hy2,Hz2])

plt.figure(2,figsize=(8,5))
plt.plot(sol.t,tau[:,0]/(tau.max()),'-',color='deepskyblue',label=r'$\tau_{x}$')
plt.plot(sol.t,tau[:,1]/(tau.max()),'-',color='slateblue',label=r'$\tau_{y}$',)
plt.plot(sol.t,tau[:,2]/(tau.max()),'-',color='chocolate',label=r'$\tau_{z}$',)
#plt.plot(sol.t,np.sqrt(tau[:,0]**2+tau[:,1]**2+tau[:,2]**2)/(tau.max()))
plt.xlabel('Time (ns)',fontsize=14)
plt.legend(fontsize=12,frameon=False)
plt.ylabel('Normalized cross-product torque',fontsize=14)

```


Appendix C: Sample Code for Toy Model Simulation

We will treat the problem of a torsion spring coupled to a linear spring. One can think of such a system of springs as a toy model for torsional eigenmodes that exhibit simultaneously torsional and translational behaviour. The toy model consists of a torsion spring with effective spring constant κ and a linear spring of spring constant k . These springs are coupled by a linear coupling spring of spring constant K . The equations of motion for coupled oscillators (torsional and linear) can be described by the following differential equations for the torsion spring:

$$I \frac{d^2\theta}{dt^2} = -(\kappa\theta + Kx_1R) + KRx_2 - \gamma_T \frac{d\theta}{dt} + \tau_D \cos \omega t \quad (\text{C.1})$$

and the linear spring:

$$m \frac{d^2x_2}{dt^2} = -(k + K)x_2 - \gamma_L \frac{dx_2}{dt} + Kx_1 \quad (\text{C.2})$$

For small angle deviations $\theta = x_1/R$, so we may write the first equation in the following way:

$$\frac{I}{R} \frac{d^2x_1}{dt^2} = -\left(\kappa \frac{x_1}{R} + Kx_1R\right) + KRx_2 - \frac{\gamma_T}{R} \frac{dx_1}{dt} + \tau_D \cos \omega t \quad (\text{C.3})$$

For this solver to do it's job we must represent the above equations as a system of four first order differential equations (this behaves also as a specification of boundary

conditions):

$$\begin{aligned}
 y_1 &= \frac{dx_1}{dt} \\
 \frac{dy_1}{dt} &= \frac{1}{I} \left[- \left(\kappa + KR^2 \right) x_1 + KR^2 x_2 - \gamma_T y_1 + R\tau_D \cos \omega t \right] \\
 y_2 &= \frac{dx_2}{dt} \\
 \frac{dy_2}{dt} &= \frac{1}{m} \left[- (k + K) x_2 - \gamma_L y_2 + K x_1 \right]
 \end{aligned}
 \tag{C.4}$$

Note: the coupling in this case is based on the size of KR

Listing C.1: Numerical solver for differential equation presented above (C.4)

```

#!/usr/bin/env python3
# -*- coding: utf-8 -*-
"""
Created on Sat Nov 15 13:41:30 2019
Adapted from ipynb version
@author: michaeldunsmore
"""

import numpy as np
from scipy.integrate import odeint
from scipy.integrate import solve_ivp
from numpy import loadtxt
import matplotlib.pyplot as plt
from matplotlib.font_manager import FontProperties

def vectorfield(omega, t, p):

    x1, y1, x2, y2 = omega
    k, kappa, K, R, gt, gl, taudrive, omega, I, m = p

    # Create f = (x1', y1', x2', y2'):
    f = [y1,
         -(kappa+K*(R**2))*x1+K*(R**2)*x2-gt*y1+R*taudrive*np.cos(omega*t)) / I,
         y2,
         -(k+K)*x2-gl*y2+K*x1) / m]
    return f

# Parameter values
#Degree of Torsionality
DoT=0.8348
# Effective Mass and Moment of Area (Comsol)
m= 1.79e-13 #kg
I= 4.78e-26 #kg m^2
# Spring Constant (Also Comsol)
kappa = 17e-12
k = kappa*m/I
epsilon = 0.1
K = epsilon*k
# Torsional resonance frequency (Hz)
omega = (1 + 0.955*epsilon)*np.sqrt(kappa/I)
# Geometric Properties
# R=3.99e-6
R = 5.17e-7 #to match assumption kappa = kR^2 (and hence also I = mR^2)
# Damping coefficients
gt = I*omega/2000
gl = m*omega/2000

#Drive Nm
taudrive=43e-17

```

```

#taudrive=0 #for looking at free ringdowns

# Initial conditions
# x1 and x2 are the initial displacements; y1 and y2 are the initial velocities
#x1 = 1e-7 #handy to turn off the drive and look at the
           #ringdown following an initial displacement
x1 = 0e-10
y1 = 0.0
x2 = 0e-10
y2 = 0.0

# ODE solver parameters
abserr = 1.0e-8
relerr = 1.0e-6
           # output a point every half radian of oscillation
Nhalfrad = 60000
stoptime = Nhalfrad/(2*omega)
numpoints = Nhalfrad

# Create the time samples for the output of the odeint solver.
t = [stoptime * float(i) / (numpoints - 1) for i in range(numpoints)]
t.span = [0, stoptime]

# Pack up the parameters and initial conditions:
p = [k, kappa, K, R, gt, gl, taudrive, omega, I, m]
omega0 = [x1, y1, x2, y2]

# Call the ODE solver.
wsol = odeint(vectorfield, omega0, t, args=(p,), atol=abserr, rtol=relerr)
#wsol = solve_ivp(vectorfield, t_span, omega0, args=(p,), atol=abserr, rtol=relerr)
print(wsol)
#with open('two_springs.dat', 'w') as f:
           # Print & save the solution.
           # for t1, w1 in zip(t, wsol):
           #     print (f, t1, w1[0], w1[1], w1[2], w1[3])

# Plot the solution that was generated

tout, x1out, y1out, x2out, y2out = [t, wsol[:,0], wsol[:,1], wsol[:,2], wsol[:,3]]

plt.figure(1, figsize=(12, 4.5))

plt.xlabel('t')
plt.grid(True)
lw = 0.5

plt.plot(tout, x1out, 'b', linewidth=lw, label='$x_1$')
plt.plot(tout, x2out, 'g', linewidth=lw, label='$x_2$')
plt.xlim([0.00100, 0.001005])
plt.legend(prop=FontProperties(size=16))
plt.title('Displacement 1 for the coupled spring-mass system')
plt.show()

plt.figure(2, figsize=(12, 4.5))

plt.xlabel('t')
plt.grid(True)
lw = 0.2
plt.plot(tout, x2out, 'g', linewidth=lw, label='$x_2$')
#plt.xlim([0.00000, 0.00005])
plt.legend(prop=FontProperties(size=16))
plt.title('Displacement 2 for the coupled spring-mass system')
plt.show()
#savefig('two_springs.png', dpi=100)

```